

Article

Enrichment of Se-Te-Au in the Jilongshan Au-Cu Skarn Deposit, Hubei Province: Insight from Pyrite Texture and Composition

Guizhou Nan ¹, Jing Xu ^{1,*} , Wenyuan Liu ¹, Suyu Chen ¹, Zhihui Cen ² and Jichen Jiang ¹¹ Zijin School of Geology and Mining, Fuzhou University, Fuzhou 350108, China; 15146@163.com (W.L.)² Central South Geological Survey Institute, China Metallurgical Geology Bureau, Wuhan 430081, China

* Correspondence: xujing3800@126.com

Abstract: Selenium and Te are two important critical metals, which are often produced as by-products in Au-Cu deposits related to magmatic-hydrothermal systems, such as porphyry and skarn deposits. The Jilongshan Au-Cu deposit is a typical skarn deposit located in the middle and lower parts of the Yangtze River metallogenic belt. Previous studies show that it has valuable Se and Te resources, but their occurrence, particularly the relationship between the texture and composition of pyrite, and the enrichment mechanism of Se, Te, and Au remain unclear. Here, the textures and the major and trace elements of the Jilongshan pyrites were studied by using an optical microscope, EMPA, and LA-ICP-MS to reveal the occurrence of Se, Te, and Au in pyrite, as well as their genetic links with the pyrite mineralogical signature. The results show that there are three types of ores in the Jilongshan deposit, including granite porphyry-hosted, skarn-hosted, and carbonate-hosted ores. All of these ores contain major amounts of pyrite, which can be divided into four different generations. The first generation of pyrite (Py1) belongs to sedimentary genesis with a typical framboid texture and its Co/ Ni ratios are less than 1, whereas Py2, Py3, and Py4 belong to hydrothermal genesis and their Co/ Ni ratios are between 1.0 and 30.2. Selenium concentrations in Py2 and Py3 are relatively high (median, 138 ppm and 344 ppm, respectively), which are mainly present as isomorphism and a small amount as selenite in pyrite. Compared with granite porphyry-hosted and skarn-hosted ores, pyrite from carbonate-hosted ores has the highest Se concentrations. The latest generation of pyrite (Py4) contains the highest concentrations of Te (average, 140 ppm) and Au (average, 12 ppm) among the hydrothermal pyrites. Therefore, the precipitation of Se mainly occurs in pyrite during the early high-temperature stage, whereas higher concentrations of Te and Au are mainly enriched in pyrite during the late stage with low temperatures.

Keywords: selenium; tellurium; gold; pyrite; enrichment mechanism; Jilongshan skarn deposit

Citation: Nan, G.; Xu, J.; Liu, W.; Chen, S.; Cen, Z.; Jiang, J. Enrichment of Se-Te-Au in the Jilongshan Au-Cu Skarn Deposit, Hubei Province: Insight from Pyrite Texture and Composition. *Minerals* **2023**, *13*, 1516. <https://doi.org/10.3390/min13121516>

Academic Editors: Jiajun Liu, Shen Gao and Giorgio Garuti

Received: 23 October 2023
Revised: 26 November 2023
Accepted: 30 November 2023
Published: 3 December 2023



Copyright: © 2023 by the authors. Licensee MDPI, Basel, Switzerland. This article is an open access article distributed under the terms and conditions of the Creative Commons Attribution (CC BY) license (<https://creativecommons.org/licenses/by/4.0/>).

1. Introduction

Critical mineral commodities are significant to sustainable development and in large demand in modern society. Therefore, the mineralization of critical mineral commodities has been highlighted in the field of mineral deposit science in China and around the world [1]. Tellurium and Se are typical disperse elements, which are usually very difficult to form during industrial enrichment. However, many types of Au deposits or Au-rich deposits mostly contain some Au, Ag, Bi, Pb, and other elements of tellurides, selenides, as well as Te and Se contents in some Au deposits to meet the requirements of industrial utilization [2,3]. The mineralization between Te, Se, and Au in such deposits should be further studied to meet the strategic needs of our country.

Pyrite, as an important carrier of Se, Te, and Au, has been extensively studied in recent years [4–11]. The trace elements of pyrite contain abundant genetic information and have become a powerful tool for determining ore genesis types, restricting the source of ore-forming materials, and inversing the evolution of metallogenic fluid [12,13]. Trace elements occur in pyrite in two different forms: (a) substitution into the crystal lattice; and

(b) nano-to-micro-scale mineral inclusions [6–8]. Based on the composition, concentrations, and correlation of trace elements in pyrite, some significant insights are proposed to define the possible enrichment mechanism and ore-forming processes (e.g., magma degassing, fluid boiling, and water–rock interaction) of Se, Te, and Au [6–10,13–15].

The Jilongshan Au–Cu deposit is a typical skarn deposit. Many studies have been reported about its deposit geology, geochronology, ore-forming fluids, and the occurrence of Au and Ag [16–20]. However, there are barely no studies in regard to the occurrence and enrichment mechanism of the critical elements in pyrite in this area, such as Se and Te. This paper focuses on a systematic petrological observation of the pyrite in the Jilongshan deposit, and we divide different generations of pyrites based on cross relationships, alteration, and associated/co-existing mineral assemblages. By using electron probe microanalysis (EMPA) and laser ablation inductively coupled plasma mass spectrometry (LA-ICP-MS), we analyze the major and trace element concentrations in the classified pyrite. It reveals the intrinsic relationship between the textures and compositions of pyrite and the enrichment of Se, Te, and Au in the Jilongshan deposit, guiding the development and utilization of critical metal commodities in the region.

2. Geological Setting

2.1. Regional Geology

The middle–lower parts of the Yangtze River is the most important Fe–Cu–Au and other polymetallic metallogenic belt in China and is located south of the Dabieshan orogen belt and north of the Yangtze Craton (Figure 1a). The Jilongshan Au–Cu skarn deposit is located at the Fengshan orefield in this metallogenic belt [16].

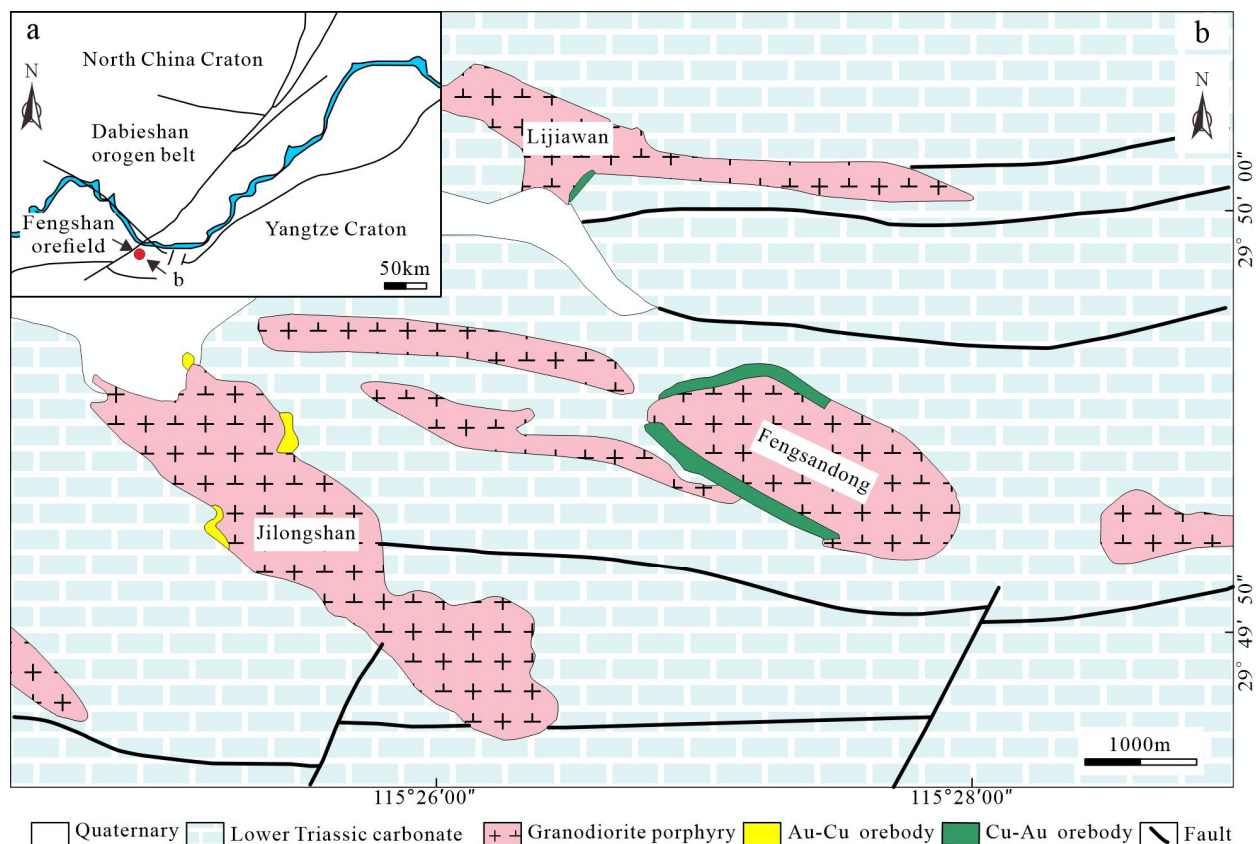


Figure 1. (a) Location of the Fengshan orefield. (b) Geological map of the Fengshan orefield, showing the distributions of the Jilongshan, Fongsandong, and Lijiawan deposits.

The Fengshan orefield mainly consists of three parts [18], including the western Jilongshan Au–Cu skarn deposit (Cu metal reserves, 279,900 tonnage; Au metal reserves,

37.09 tonnage), the eastern Fengsandong Cu porphyry-skarn deposit (Cu metal reserves, 504,600 tonnage), and the northern Lijiawan Au skarn deposit (Cu metal reserves, 98,100 tonnage; Au metal reserves, 5.61 tonnage) (Figure 1b). The stratigraphic sequence in the Fengshan area is exposed from the Silurian to the Quaternary, is relatively well-developed, and is composed of dolomitic limestone, dolomite, limestone, shale, and sandstone. Major structures in the area include a series of close to parallel ENE–EW trending transtensional faults and EW trending faults. The main intrusions and ore occurrences in the area are distributed along the faults, which play a significant role in controlling the intrusions and skarn mineralization [16,19]. There are frequent magmatic activities in the region, mostly in the Yanshan period intrusive activities. The molybdenite Re-Os isotopic model age ranges from 147.7 ± 2.4 to 151.6 ± 4.02 Ma with an isochron age of 148.6 ± 1.5 Ma. The intrusive rocks are mainly diorite, quartz diorite (138.2 ± 1.8 Ma), and granodiorite porphyry (151.6 ± 0.7 Ma) [20,21]. Skarn Au and Cu mineralization is mainly related to the quartz diorite and granodiorite porphyry in the region.

2.2. Deposit Geology

The Jilongshan deposit is controlled by the Jilongshan intrusion, Lower Triassic carbonatite, and faults (Figure 2a). The exposed strata in the mining area are relatively simple and mainly consist of the Lower Triassic carbonates including limestone, dolomitic limestone, and marble, except for the Quaternary. The magmatic rocks are mainly granodiorite porphyry, with a marginal phase of quartz diorite porphyry [18]. Previous studies on zircon U-Pb in the granodiorite porphyry have shown the age of 151.6 ± 0.7 Ma, indicating that it is formed during the Early Jurassic–Late Cretaceous. It is consistent with the mineralization age obtained with Re-Os isotope geochronology (148.6 ± 1.5 Ma) of molybdenite in the skarn, indicating that skarn mineralization is related to the intrusion [19–21].

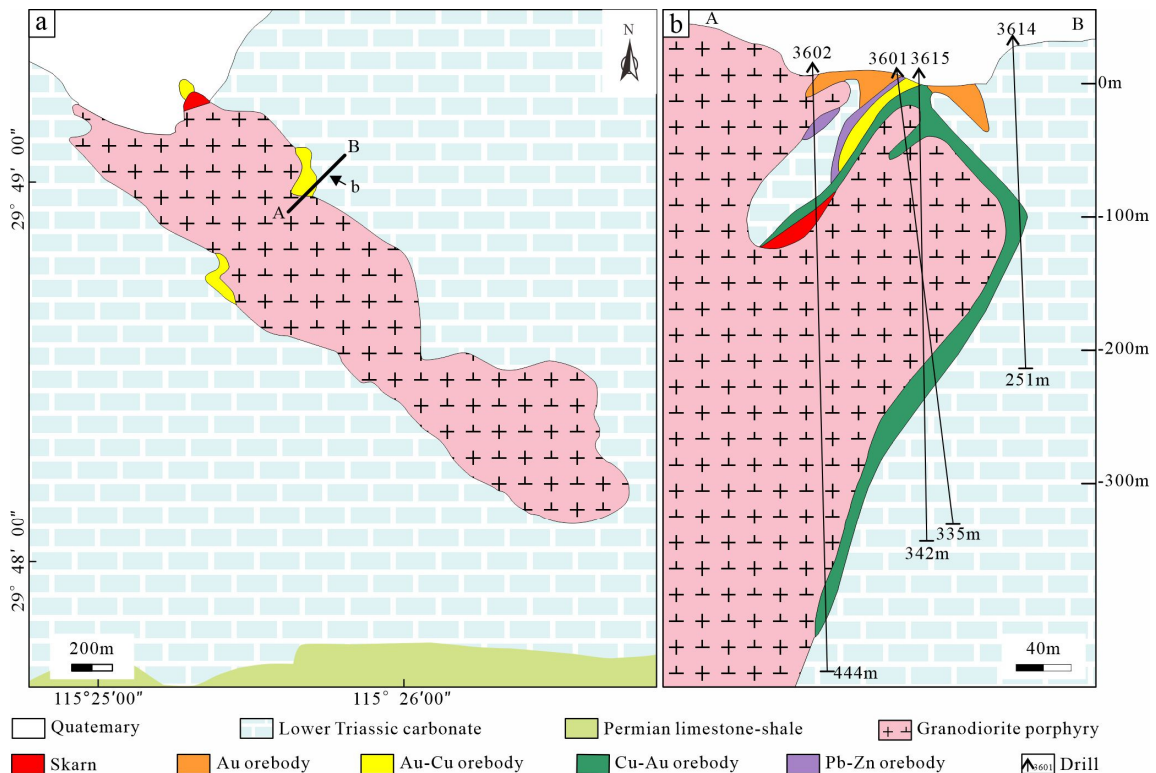


Figure 2. Geological map of the Jilongshan deposit (a), and related geological section profile (b).

The orebodies mainly exist in the contact zone between the granodiorite porphyry and Lower Triassic carbonates, with a small amount located in the interlayer fracture zone. The occurrence and spatial distribution of the orebodies are mainly controlled by

NW-NWW trending faults. Skarn-type Au-Cu ore is the dominating mineralization style, and minor porphyry-type and carbonate-type ores are also developed in the Jilongshan deposit (Figure 3). The ore composition is relatively complex, and the main ore minerals are pyrite, chalcopyrite, bornite, pyrrhotite, covellite, sphalerite, galena, and gold, with a small amount of Te-Bi-Ag minerals. The alteration is strongly developed in the deposit, mainly including skarn, carbonatization, silicification, chlorization, and potassium [18].

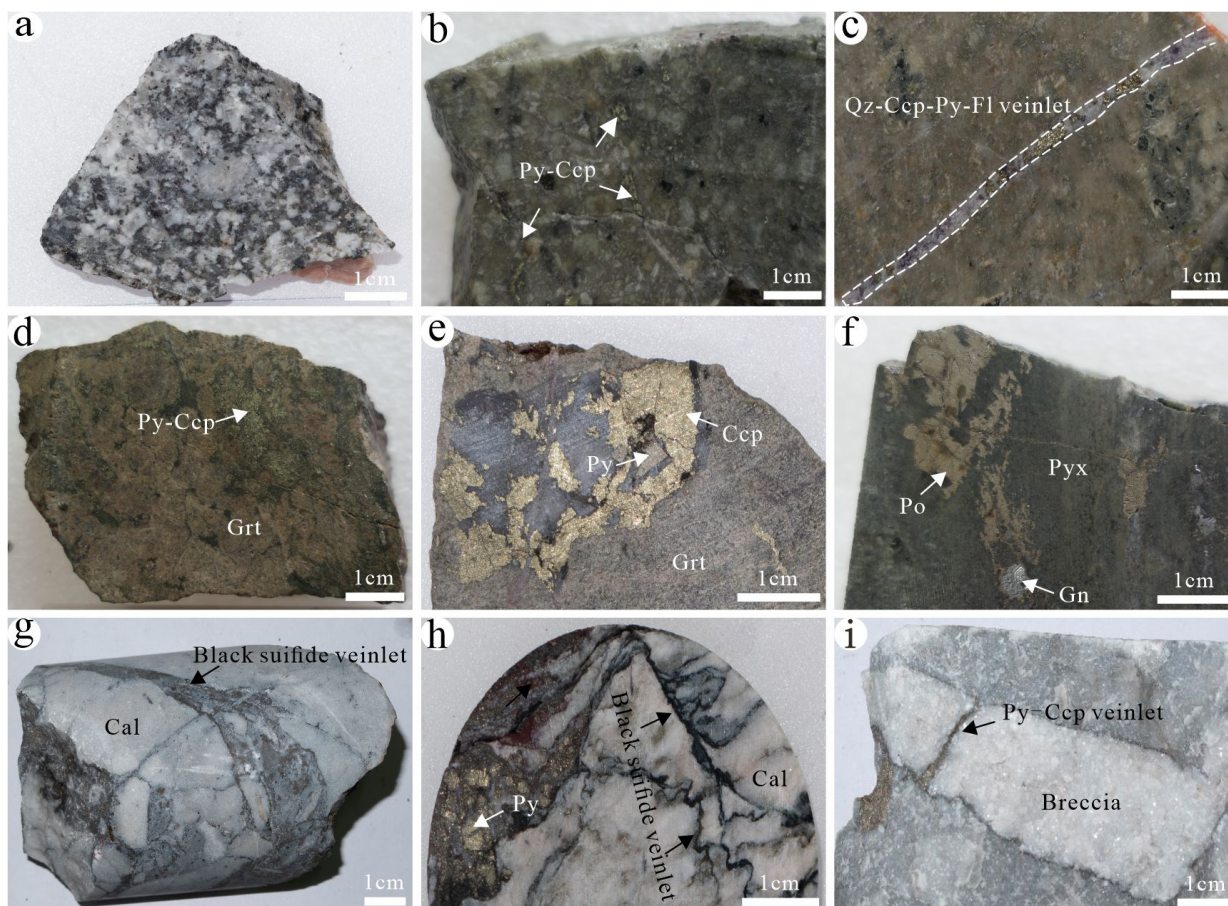


Figure 3. Petrography of ore types in the Jilongshan deposit. (a) Unaltered granodiorite porphyry; (b) pyrite–chalcopyrite veinlets in altered granodiorite porphyry; (c) pyrite–chalcopyrite–quartz–fluorite veinlets in potassic granodiorite porphyry; (d) agglomerated pyrite–chalcopyrite in red-brown garnet-dominated skarn; (e) agglomerated pyrite–chalcopyrite in garnet skarn; (f) galena and pyrrhotite in pyroxene skarn; (g) carbonate breccia filled and cemented by irregular black sulfide veinlets; (h) pyrite in carbonate with the occurrence of irregular black sulfide veinlets; (i) pyrite veinlets developed at the margins of carbonate breccia. Mineral abbreviations: Cal—calcite, Ccp—chalcopyrite, Fl—fluorite, Gn—galena, Grt—garnet, Po—pyrrhotite, Py—pyrite, Pyx—pyroxene, Qz—quartz.

Jilongshan Au-Cu mineralization can be divided into four stages based on cross-cutting relationships and mineral assemblages according to previous studies [18], namely, the skarn stage, retrograde stage, quartz-sulfide stage, and carbonate stage. Obvious mineralization zones have been identified in the Jilongshan deposit [19]. Vertically, the contact zone below the intrusion and wall rock is dominated by Au-Cu skarn ore bodies, whereas the contact zone above the intrusion and wall rock has hydrothermal metasomatic-type Au-Pb-Zn polymetallic ore bodies and Au ore bodies. Horizontally, Au-Cu skarn ore bodies exist in the inner contact zone close to the Jilongshan intrusion, while hydrothermal metasomatic-type Au or Au-polymetallic ore bodies appear in the outer contact zone far from the Jilongshan intrusion [19].

3. Materials and Methods

Fifty samples used in this study were mainly collected from ore piles and partially from drill cores, with the types of ore mainly including skarn-hosted, porphyry-hosted, and carbonate-hosted, which cover all ore types in the mining area. Many of our samples come from ore piles, which makes it difficult to pinpoint the exact location of the samples.

The EPMA was carried out at the State Key Laboratory for Research on the Mechanism of Endogenous Metallic Mineralization at Nanjing University and the EPMA Laboratory of the Zijin School of Geology and Mining at Fuzhou University. Both laboratories were equipped with the EPMA model JXA-8230, with an accelerating voltage of 15 kV, a beam current of 20 nA, and a beam spot of 5 μm . Standards used were as follows: S (FeS_2), Fe (FeS_2), As (FeAs_2), Au (AuTe_2), Ag (AgBiSe_2), Te (AuTe_2), Se (CuS), Pb (PbS), Co (Co), and Ni (NiS). X-ray lines were as follows: S ($\text{K}\alpha$), Fe ($\text{K}\alpha$), As ($\text{L}\alpha$), Au ($\text{L}\alpha$), Ag ($\text{L}\alpha$), Te ($\text{L}\alpha$), Se ($\text{L}\alpha$), Pb ($\text{M}\alpha$), Co ($\text{K}\alpha$), and Ni ($\text{K}\alpha$). Minimum detection limits (for pyrite) were (2σ): S (62 ppm), Fe (178 ppm), As (266 ppm), Au (282 ppm), Ag (143 ppm), Te (166 ppm), Se (131 ppm), Pb (189 ppm), Co (161 ppm), and Ni (156 ppm), with variable element peak analysis times depending on the characteristics of the mineral elements.

Trace element tests by LA-ICP-MS of the representative pyrite grains were done respectively at the Guangzhou Tuoyan Analytical Technology Co., Ltd., Guangzhou, China, and the Center for Research on the Genesis and Exploration Techniques of Ore Deposits of Hefei University of Technology's Laboratory for Mineral Micro-Area Analysis. The model of the former is an NWR 193 nm ArF Excimer laser-ablation system coupled to an iCAP RQ (ICPMS). Helium (700 mL/min) was applied as a carrier gas. The ablated aerosol was mixed with Ar (890 mL/min) as a transport gas before exiting the cell. Trace element compositions of the samples are calibrated against various reference materials (NIST SRM610 and MASS-1) without using an internal standard. The laser fluence was 3.5 J/cm², with a repetition rate of 6 Hz, a 30 μm spot size, and an analysis time of 45 s, followed by a 40 s background measurement. IOLITE was used to analyze the data. The sulfide standards SRM612 and GE7b were used as the unknown sample to evaluate the data quality. The laser ablation system of the latter is Cetac Analyte HE, and the ICP-MS is Agilent 7900. It was used as a carrier gas and argon as a make-up gas to adjust sensitivity during laser ablation. Sulfide trace element concentration was quantitatively calculated using multiple reference standards (NIST610, NIST612, BCR-2G) and sulfide standard (MASS-1) as methods for multi-external standard single internal standard. Minimum detection limits of the selected elements are Co (0.30 ppm), Ni (0.49 ppm), Cu (0.45 ppm), Zn (0.90 ppm), Ge (0.62 ppm), As (1.93 ppm), Se (0.78 ppm), Ag (0.01 ppm), Cd (0.04 ppm), Sb (0.20 ppm), Te (0.10 ppm), Au (0.01 ppm), Tl (0.01 ppm), Bi (0.01 ppm), and Pb (0.01 ppm).

4. Results

4.1. Different Types of Ores and Related Petrography

Three types of ores, including porphyry-type, skarn-type, and carbonate-type, have been identified in the Jilongshan deposit (Figure 3), and the following is a description of these different types of ores and related mineral assemblages, particularly the pyrites (Table S1).

(1) Porphyry-type ore: It mainly occurs in the granodiorite porphyry in the shallow part of the deposit. The granodiorite porphyry is gray and gray-white in color. It mainly consists of quartz, plagioclase, amphibole, K-feldspar, and biotite. Sericitization, silicification, pyritization, and potassium are major alterations within the granodiorite porphyry. A small amount of sulfides, quartz, and fluorite occur in the granodiorite porphyry as veinlets (Figure 3b,c). Pyrite is the main ore mineral, and a small amount of chalcopyrite is also locally visible. The types of pyrite include majorly Py2 and minorly Py3 (see below).

(2) Skarn-type ore: It is the main ore type in the Jilongshan deposit. Sulfides occur in the skarn-type ore as veinlets, are disseminated, and have massive texture (Figure 3d–f). The skarn minerals are composed of garnet and pyroxene. Minorly actinolite, epidote, and chlorite also appear locally. The ore minerals are mainly composed of pyrite, chalcopyrite, magnetite, pyrrhotite, sphalerite, galena, minor tetrahedrite, and bornite. The types of

pyrites are mainly Py2 and Py4 (see below). It is worth noting that a small amount of modified Py1 locally remains in the core of Py2.

(3) Carbonate-type ore: It is mainly hosted in the distal marble and related carbonates. The quartz-sulfide mineral assemblages are seen as veins interspersed with limestone (marble) or cemented formation breccia (Figure 3g–i). The ore minerals mainly include tetrahedrite, chalcopyrite, pyrite, galena, and sphalerite. Calcite is the major gangue mineral. A large number of Py1 and Py4 occur in this type of ore (see below).

4.2. Pyrite Types and Generational Characteristics

Reflected light microscopy was completed on all the samples to determine the mineral textures, assemblages, and cross-cutting relationships among sulfides. The pyrites studied in this paper are classified into four generations. As description above, different generations of pyrites can occur in the same rock type. Similarly, different types of rocks can contain the same type of pyrite. Therefore, there is absolutely no correspondence between the pyrite generations and rock types. Here, the classification of the Jilongshan pyrite is mainly defined according to pyrite sequences. They are characterized as follows:

(1) Framboidal pyrite (Py1): It is composed of submicron pyrite or microcrystals of equal grain size, which resemble a strawberry. It formed during the sedimentary period, mainly existing in black carbonaceous, muddy impure carbonate rocks. Observed under the microscope, the diameter of framboidal pyrites varies from 9.7 μm to 44.5 μm (Figures 4a–d and 5a,b). Some framboidal pyrites are surrounded by larger euhedral and subhedral pyrites (Py2) (Figure 4a,e), representing Py1 formation in the early sediment diagenesis. Some galena, sphalerite, and tetrahedrite, which formed during the later hydrothermal stage, can be locally observed around Py1 (Figure 4d).

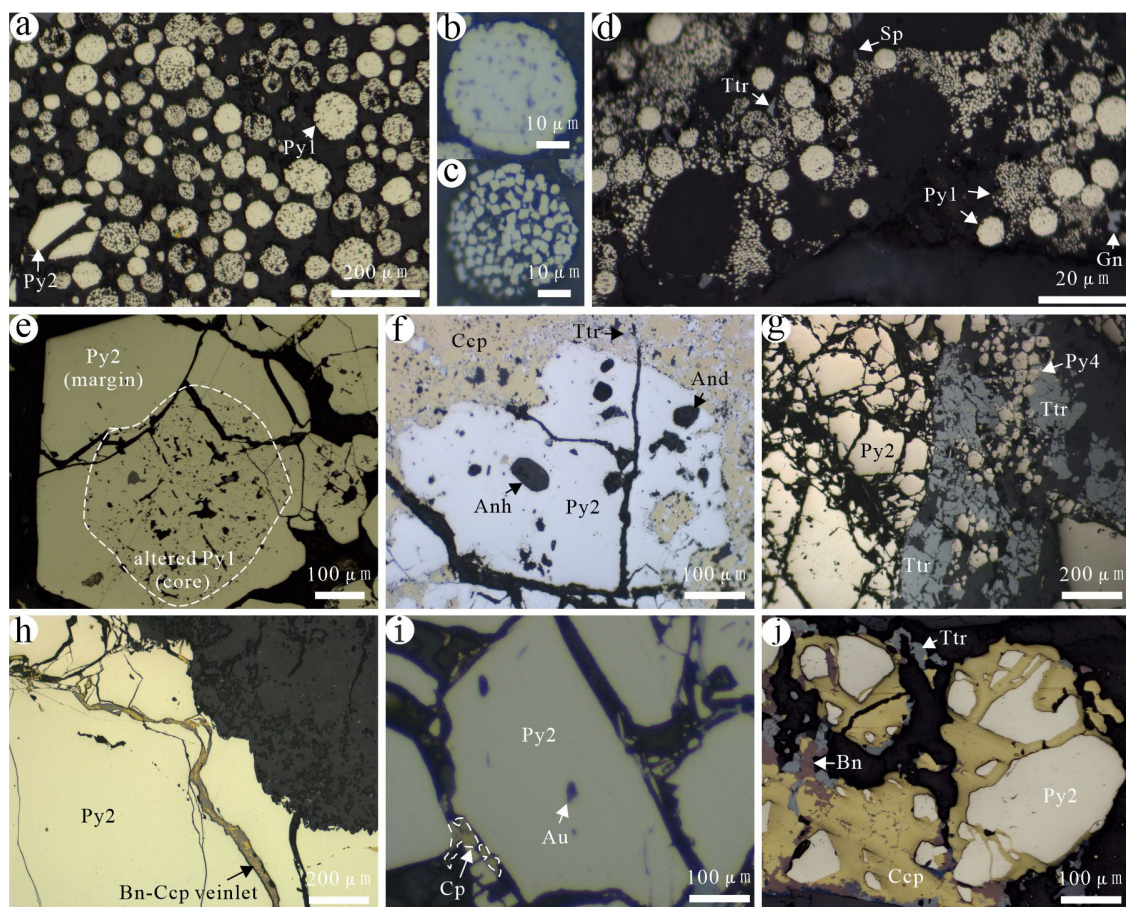


Figure 4. Characteristics of different generations of pyrite in the Jilongshan deposit. (a) Framboidal pyrite (Py1) formed in the sedimentary period and a small amount of hydrothermal Py2; (b) single

framboidal with tight microcrystals; (c) single framboidal pyrite with large gaps between the microcrystals; (d) framboidal pyrite and surrounding microcrystals; (e) a ring of hydrothermal Py2 developed around altered Py1; (f) Py2 containing anhydrite and andalusite inclusions and replaced by chalcopyrite; (g) the replacement of Py2 by later Py4 and tetrahedrite; (h) chalcopyrite–bornite veinlets cross-cutting Py2; (i) Py2 containing native Au, which was confirmed by EDS data even though the color is not golden yellow; (j) Py2 replaced by chalcopyrite, bornite, and tetrahedrite. Mineral abbreviations: And—andalusite; Anh—anhydrite; Au—native gold; Bn—bornite; Ccp—chalcopyrite; Py—pyrite; Ttr—tetrahedrite.

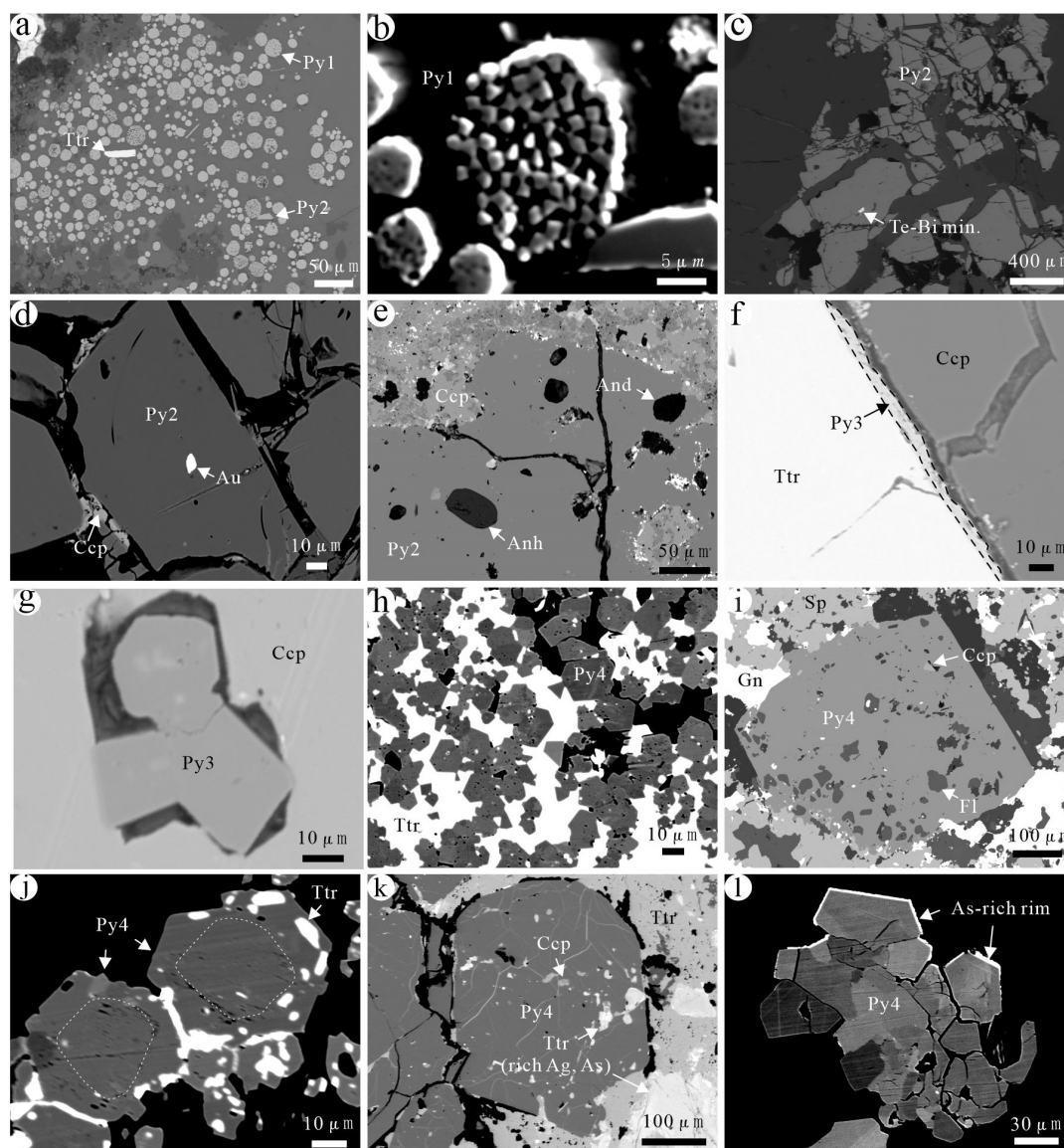


Figure 5. Backscattering characteristics of different generations of pyrite in the Jilongshan deposit. (a) Framboidal pyrite (Py1) and little Py2; (b) different shape microcrystals of Py1; (c) fissure development in Py2; (d) native gold in Py2; (e) some gangue minerals in Py2; (f) Py3 on the edge of chalcopyrite; (g) Py3 inside chalcopyrite and some inclusions in Py3; (h) intergranular spaces of Py4 grains filled with tetrahedrite; (i) chalcopyrite and fluorite in Py4; (j) Py4 has obscure zonation and was strongly replaced by tetrahedrite; (k) cracks of Py4 grains filled with tetrahedrite; note that Ag- and As-bearing tetrahedrites have brighter BSE images; (l) As-rich edge of Py4. Mineral abbreviations: And—andalusite; Anh—anhydrite; Au—gold; Ccp—chalcopyrite; Fl—fluorite; Gn—galena; Py—pyrite; Sp—sphalerite; Ttr—tetrahedrite.

(2) Early-stage hydrothermal pyrite (Py2): It is formed during the early high-temperature stage of hydrothermal fluids. It widely occurs in the porphyry-type, skarn-type, and carbonate-type ores. This pyrite exhibits coarse grains, mostly subhedral to anhedral, with local strong fragment and cleavage development (Figures 4e–g,j and 5c–e). It is widely replaced by subsequent sulfides, such as chalcopyrite, bornite, hematite, electrum, hessite, matildite, and tetrahedrite (Figures 4h,j and 5d). Native Au is found in Py2 (Figure 4i), and internally some gangue mineral inclusions are present like gypsum, andalusite, and fluorite, which are confirmed by electron spectrum analysis (Figures 4f and 5e).

(3) Late-stage hydrothermal pyrite (Py3): It is formed later than Py2 and is mainly distributed in carbonates with mostly subhedral to anhedral fine grains. It is formed later than chalcopyrite and exists along the edges of chalcopyrite or fills in its cracks (Figures 5f,g and 6a–d). A small amount of Py3 in chalcopyrite coexists with tetrahedrite (Figures 5g and 6a).

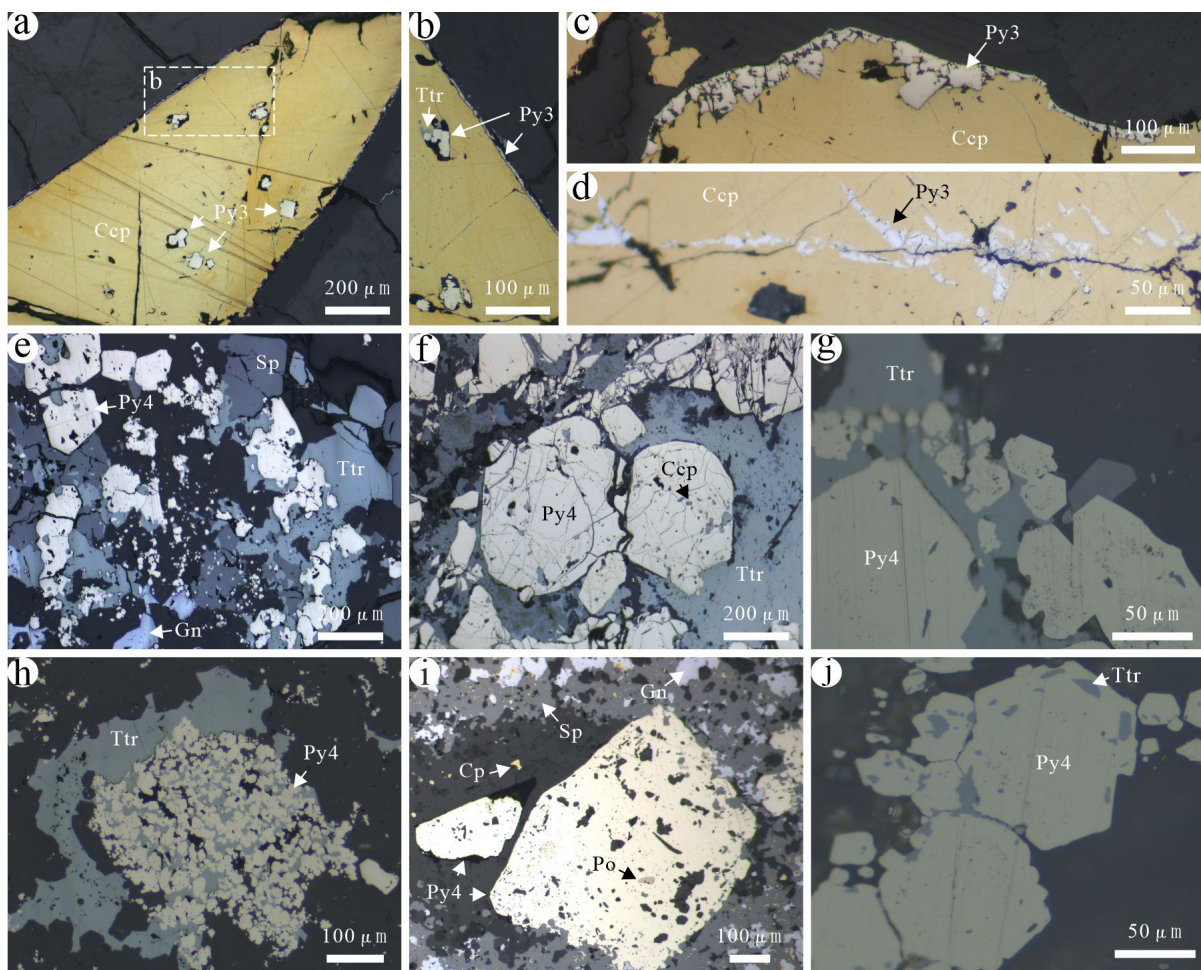


Figure 6. Characteristics of different generations of pyrites in the Jilongshan deposit. (a) Euhedral or subeuhedral Py3 developed in chalcopyrite; (b) insert from (a) showing detailed Py3 occur in both inside and edge of chalcopyrite, note the pore and mineral inclusions in chalcopyrite indicating the replacement chalcopyrite by Py3 and tetrahedrite; (c,d) Py3 developed at both the edge of chalcopyrite and in the internal fractures; (e) Py4–sphalerite–galena–tetrahedrite assemblage; (f) tetrahedrite developed in the fractures of Py4 with minor chalcopyrite; (g,h) Py4 filled with tetrahedrite between grains; (i) galena, sphalerite, and chalcopyrite developed around Py4, pyrrhotite in Py4; (j) tetrahedrite in Py4. Mineral abbreviations: Ccp—chalcopyrite; Gn—galena; Py—pyrite; Po—pyrrhotite; Sp—sphalerite; Ttr—tetrahedrite.

(4) Low-temperature pyrite (Py4): It is formed at the latest stage and is primarily observed in carbonate. A small amount of Py4 was formed by recrystallization or secondary enlargement of early framboidal pyrite (Figures 5h–l and 6g,h,j). It is often associated with tetrahedrite, galena, and sphalerite (Figures 5i–k and 6e–j). A small amount of pyrrhotite is identified in Py4 (Figure 6i). In addition, coloradoite, orpiment, and realgar are associated with Py4 [18].

4.3. EMPA Analyses

A total of 81 EMPA analyses were conducted on pyrite grains representing different generations. The results show that S concentrations of pyrites range from 47.26 wt.% to 53.73 wt.%, and Fe concentrations of pyrites range from 38.44 wt.% to 47.80 wt.% in the Jilongshan Au-Cu skarn deposit (Table 1). Moreover, different generations of pyrite contain varied Au, Se, and Te concentrations: the concentrations of Pb, As, and Te are the highest in Py1, averaging 0.26 wt.%, 1.13 wt.%, and 0.19 wt.%, respectively; Py2 is the purest and the concentrations of Te and Ni are below the detection limit; Se and Ag concentrations in Py3 are the highest, averaging 0.06 wt.% and 0.27 wt.%, respectively; Te concentration in Py4 is below the detection limit.

Table 1. EPMA data for pyrite in the Jilongshan deposit (wt.%).

Types		Fe	S	Pb	As	Te	Ag	Ni	Co	Au	Se	Total
Py1 (n = 19)	Max	46.98	52.60	1.99 *	4.94	0.28 *	0.69 *	0.04	0.11	0.13	0.04	99.49
	Min	40.93	47.26	0.02	0.06	0.03	0.02	0.02	0.02	0.03	0.02	97.11
	Median	45.47	51.39	0.21	0.89	0.26	0.05	0.04	0.06	0.08	0.03	98.13
	Mean	45.13	51.25	0.54	1.19	0.19	0.17	0.03	0.06	0.08	0.03	98.11
Py2 (n = 14)	Max	47.80	53.49	0.07	0.08	<dl	0.05	<dl	0.06	0.14	0.03	101.01
	Min	45.55	51.77	0.07	0.04	<dl	0.04	<dl	0.02	0.06	0.02	97.55
	Median	46.15	52.19	0.07	0.06	<dl	0.04	<dl	0.04	0.08	0.02	98.40
	Mean	46.24	52.46	0.07	0.06	<dl	0.04	<dl	0.04	0.09	0.02	98.81
Py3 (n = 20)	Max	47.12	53.23	0.16	0.23	0.03	1.37 *	0.11	0.09	0.10	0.23 *	100.42
	Min	43.67	50.59	0.02	0.03	0.02	0.02	0.02	0.02	0.09	0.02	97.38
	Median	46.35	52.50	0.08	0.10	0.02	0.08	0.04	0.04	0.09	0.05	99.04
	Mean	46.02	52.38	0.08	0.12	0.02	0.27	0.04	0.04	0.09	0.06	98.97
Py4 (n = 28)	Max	47.03	53.73	0.25	2.73	<dl	0.51 *	0.07	0.18	0.08	0.07	100.68
	Min	38.44	49.16	0.03	0.03	<dl	0.02	0.02	0.02	0.03	0.02	98.26
	Median	46.45	52.79	0.04	0.07	<dl	0.05	0.02	0.04	0.05	0.04	99.51
	Mean	46.07	52.70	0.08	0.31	<dl	0.09	0.04	0.05	0.05	0.04	99.51

Note: <dl, below detection limit; *, data affected by mineral inclusions. The full dataset is given in Table S2.

4.4. LA-ICP-MS Analyses

A total of 78 LA-ICP-MS spot analyses (Py1, n = 16; Py2, n = 26; Py3, n = 15; and Py4, n = 21) were completed in this study for four generations of pyrites. These spot analyses were conducted to figure out the concentrations of different trace elements. It is difficult to avoid some micro- to submicro-mineral inclusions in the pyrites, which may explain some of the outliers. So, we show the LA-ICP-MS time-resolved depth profiles in different generations of pyrites (Figure 7). Mineral inclusions such as Ag-Bi, native Au, Pb-Bi, Se-Ag, and Te-Au-Ag may occur in the Jilongshan pyrites. It should be noted that during the LA-ICP-MS data process, we tried to avoid these mineral inclusions, and the detailed data are listed in Table S3. The data for all pyrites except for Py1 that were affected by mineral inclusions are excluded from Table 2 and subsequent plots (Figures 8, 9, 11, 12 and 14).

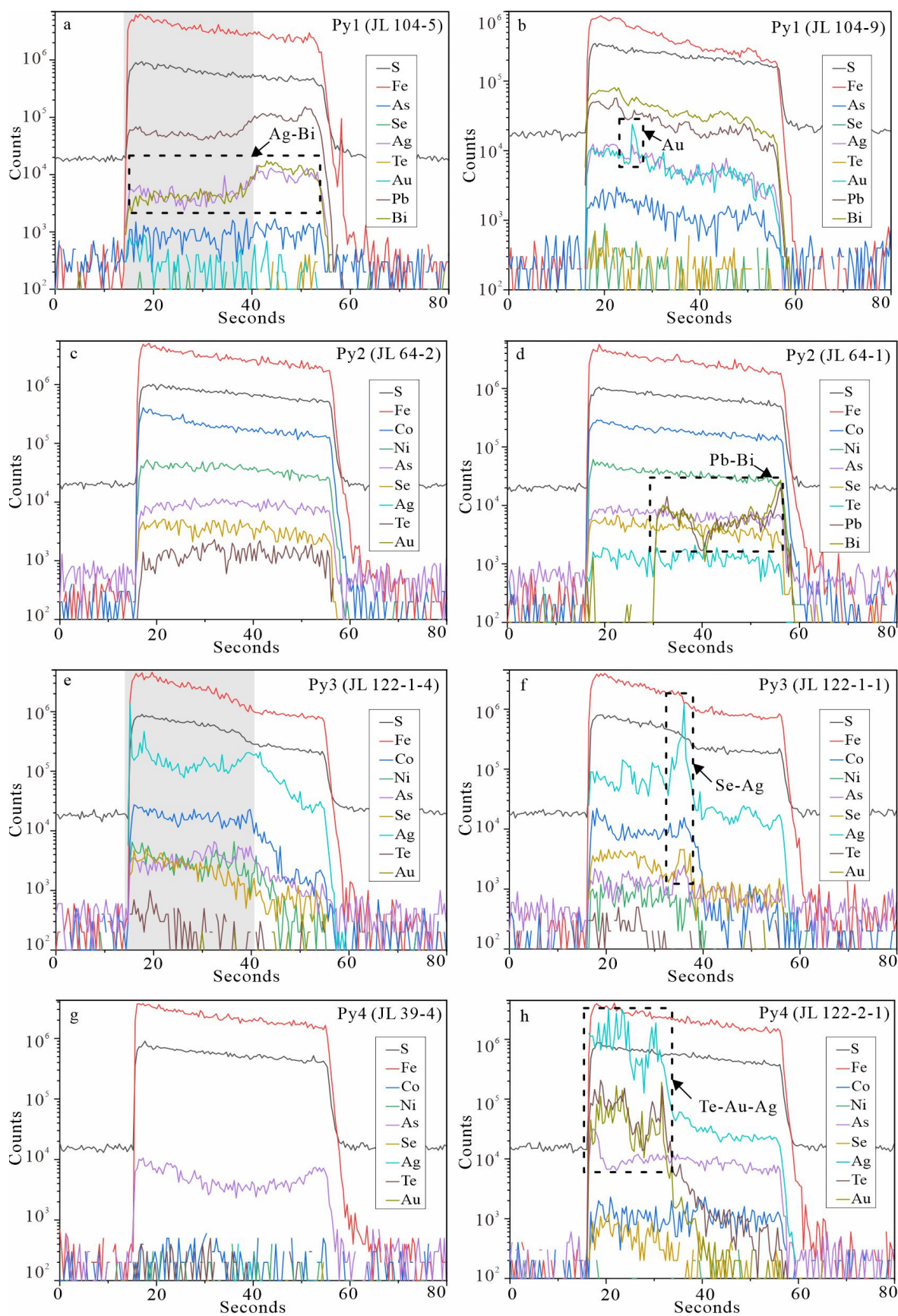


Figure 7. Representative LA-ICP-MS depth spectra of four generations of pyrites in the Jilongshan deposit. (a) Se, Te, and Au occurring in the form of isomorphisms. The same changing trend of Ag

and Bi indicating the presence of Ag/Bi micro- and/or nano-inclusions; (b) The spiky signal of Au indicating the presence of Au micro- and/or nano-inclusions; (c) Se, Te, and Au occurring in the form of isomorphisms; (d) the same changing trend of Pb and Bi indicating the presence of Pb/Bi micro- and/or nano-inclusions; (e) Se, Te, and Au occurring in the form of isomorphisms; (f) the spiky signals of Se and Ag indicating the presence of Se-Ag micro- and/or nano-inclusions; (g) Se, Te, and Au occurring in the form of isomorphisms; (h) the spiky signals of Te, Au, and Ag indicating the presence of Te-Au-Ag micro- and/or nano-inclusions. The gray areas in (a,e) refer to the effective denudation time for data calculation, which means the final data in the table are out of the effect from mineral inclusions.

Table 2. LA-ICP-MS data for pyrite in the Jilongshan deposit (ppm).

		Co	Ni	Cu	Zn	Ge	As	Se	Ag	Cd	Sb	Te	Au	Tl	Bi	Pb
Py1 * (n = 16)	Max	1.1	4.7	5481	17,116	11	88,106	23	5197	1419	6068	10,105	726	3618	4.3	19,189
	Min	1.1	3.7	991	8.1	5.1	17,548	15	656	8.5	785	407	28	890	0.40	3600
	Median	1.1	4.2	3440	74	7.0	31,149	20	1902	23	1992	2163	142	2480	0.87	13,654
	Mean	1.1	4.2	3408	1795	7.4	44,319	20	2483	159	2940	3682	256	2158	1.4	12,529
Py2 (n = 26)	Max	1102	797	138	269	7.0	1667	924	17	<dl	3.7	208	0.09	0.05	89	98
	Min	4.2	1.8	3.2	11	1.7	5.6	8.1	0.06	<dl	0.59	1.6	0.00	0.01	0.03	0.00
	Median	135	23	7.0	118	5.4	182	138	2.1	<dl	0.95	30	0.05	0.02	3.0	3.1
	Mean	294	187	24	129	5.1	393	244	4.5	<dl	1.7	47	0.05	0.02	18	13
Py3 (n = 15)	Max	652	274	<dl	2728	6.1	865	613	944	306	122	9.2	0.80	34	21	179
	Min	34	13	<dl	2327	4.9	26	201	88	17	0.76	3.3	0.11	0.22	0.53	15
	Median	194	66	<dl	2626	5.3	159	344	234	40	41	4.9	0.52	0.80	2.4	62
	Mean	248	83	<dl	2560	5.4	297	345	334	83	54	6.0	0.46	8.6	4.7	75
Py4 (n = 21)	Max	216	164	830	259	9.7	3031	388	550	70	468	494	145	230	56	618
	Min	1.7	1.3	1.9	4.8	4.3	109	0.20	0.10	1.3	0.68	3.2	0.08	0.01	0.00	2.4
	Median	5.7	8.5	119	29	5.7	1008	114	20	2.9	31	90	2.9	2.0	0.69	133
	Mean	39	23	287	65	5.8	1292	165	70	12	100	140	12	28	6.5	162

Note: <dl, below detection limit. The full dataset is given in Table S3. Because Py1 is framboidal pyrite and the grains are very fine, it is difficult to exclude all data which are affected by inclusions, so all data here are shown as Py1*.

In all generations of pyrites, the Se concentrations (median) are Py1 (20 ppm), Py2 (138 ppm), Py3 (344 ppm), and Py4 (114 ppm), respectively. The Te concentrations (median) are Py1 (2163 ppm), Py2 (30 ppm), Py3 (4.9 ppm), and Py4 (90 ppm). The Au concentrations (median) are Py1 (142 ppm), Py2 (0.05 ppm), Py3 (0.52 ppm), and Py4 (2.9 ppm). Different generations of pyrites show significant variations in trace element concentrations (Figure 8). The concentrations of trace elements including Cu, As, Ag, Sb, Te, Au, Tl, and Pb in Py1 are the highest compared with those in Py2, Py3, and Py4. Compared with Py1, Co, Ni, and Se contents gradually increase in Py2, however other trace element contents decrease. The contents of Zn and Se in Py3 are the highest among the four generations of pyrites. The contents of Te and Au in Py4 gradually increase compared with those in Py2 and Py3. In addition, the dataset shows a good positive correlation of Se vs. Ni in Py2 and Py3, Se vs. Co in Py4, and Te vs. Au in Py1 and Py4 (Figure 9b,d,e). There is also a negative correlation of Se vs. Au and Se vs. Te in Py4 (Figure 9a,c,f). Further, in this study, LA-ICP-MS spot analyses were also performed on different positions of some individual pyrite grains, and thus, the changes in trace element contents in the same pyrite grains during the formation process were observed, and the results are shown in Figure 10.

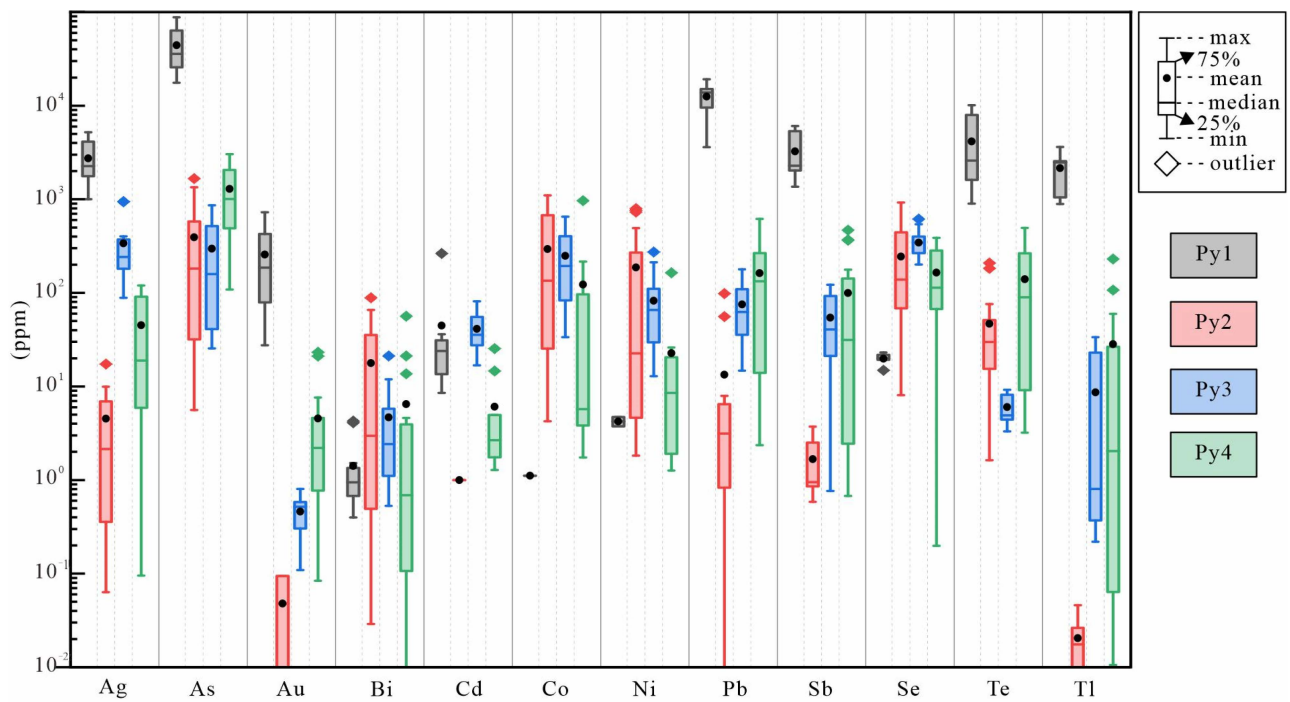


Figure 8. Box plot of the trace element concentrations in four generations of pyrites in the Jilongshan deposit.

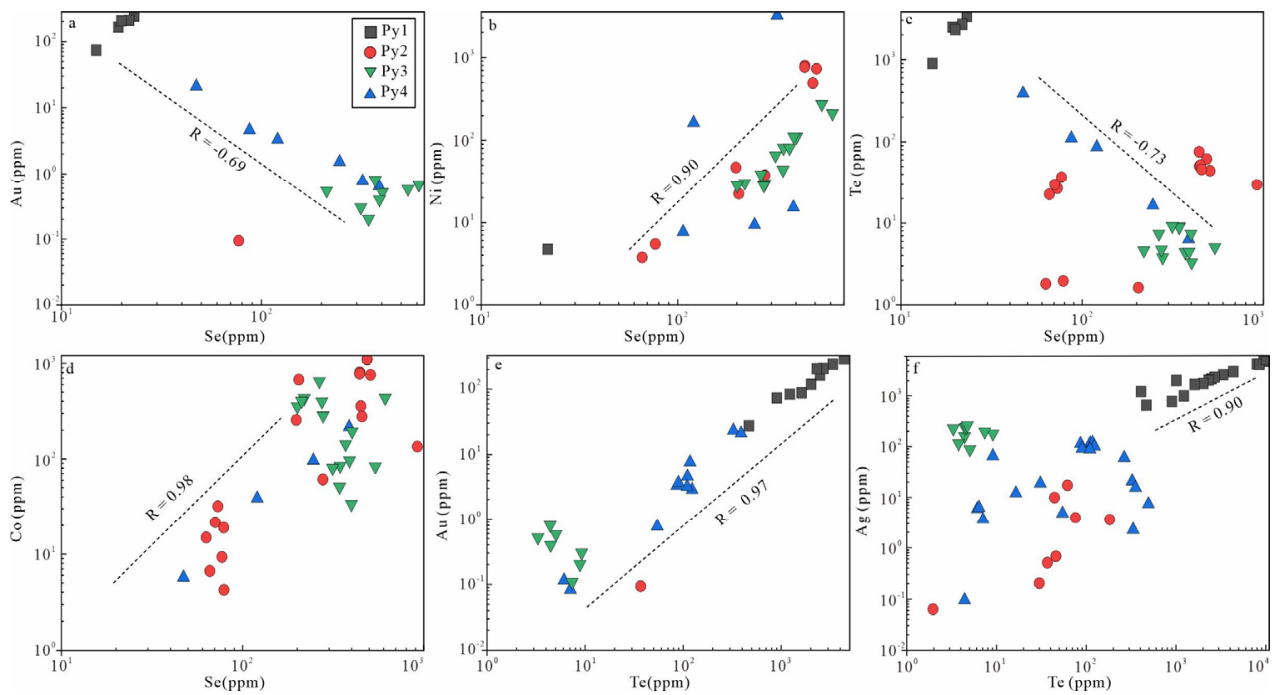


Figure 9. Correlation relationships and concentrations of some trace elements in pyrites in the Jilongshan deposit.

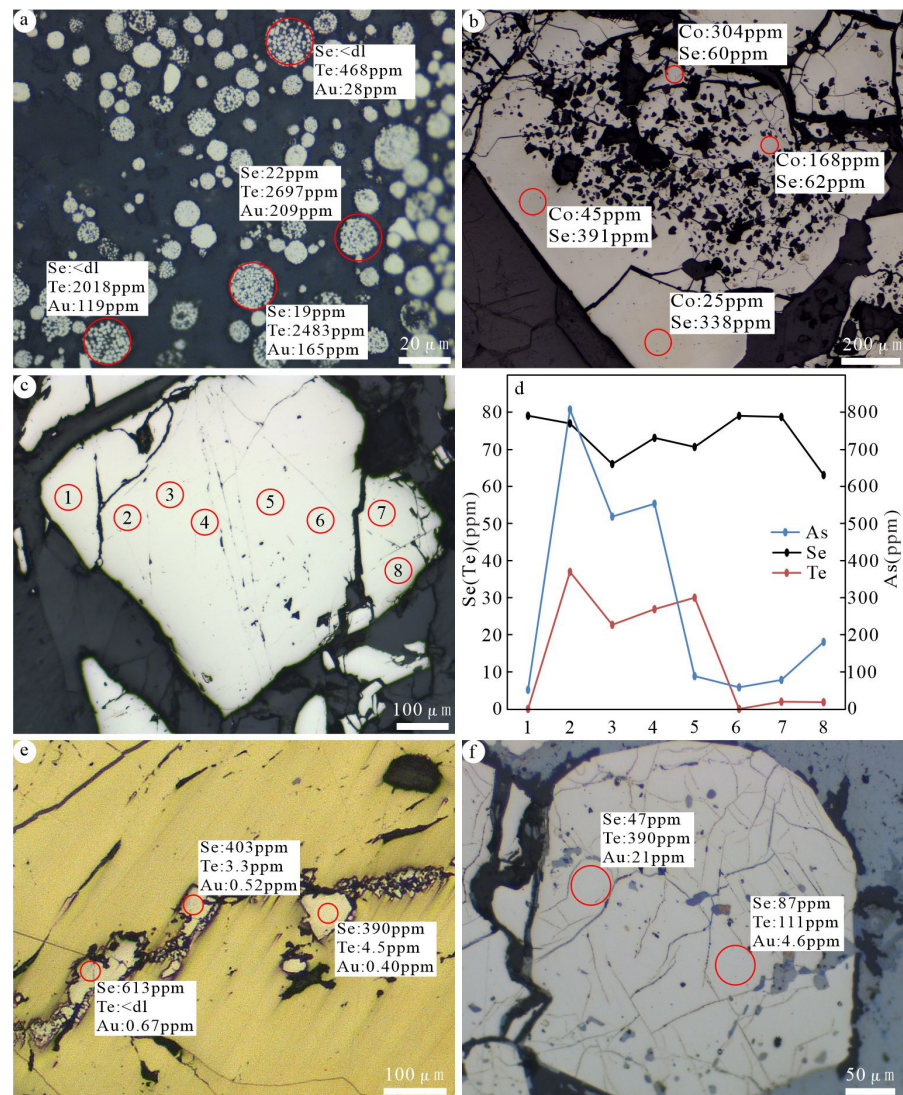


Figure 10. Characteristics of changes in trace element concentrations of representative pyrite in the Jilongshan deposit. (a) The concentrations of Se, Te, and Au in framboidal pyrite (Py1); (b) comparison of concentrations of Se and Co between Py1 and Py2; (c,d) the changes in concentrations of Se and Te in Py2, and numbers (1–8) refer to different LA-ICP-MS spot analysis locations; (e) the changes in concentrations of Se, Te, and Au in Py3; (f) the changes in concentrations of Se, Te, and Au in Py4. These numbers represent different LA-ICP-MS spots.

Principle component analysis (PCA) has become an important tool to simplify and reduce the dimensions of high dimensional multivariate datasets. There are some studies on differentiating geological samples with similar characteristics using PCA [22,23]. According to the results of LA-ICP-MS, we tried to classify pyrite using the PCA method and the result is exhibited in Figure 11. The characteristics of the trace elements can be reflected in the PCA results as the analysis points of Py1, Py2, Py3, and Py4 are clustered in different regions (Figure 11a), respectively. In the loading plot, the analyzed trace elements of pyrites seem to be grouped into three groups according to their correlation: Group 1 (Cd, Ge, Te, Pb, Au, Ag, Tl, As, and Sb), Group 2 (Co, Ni, and Se), and Group 3 (Bi) (Figure 11b). However, as the effect of mineral inclusions on Py1 cannot be excluded, the PCA plot for Group 1 and Py1 represent the elements in mineral inclusions, instead of the crystal structure of pyrite.

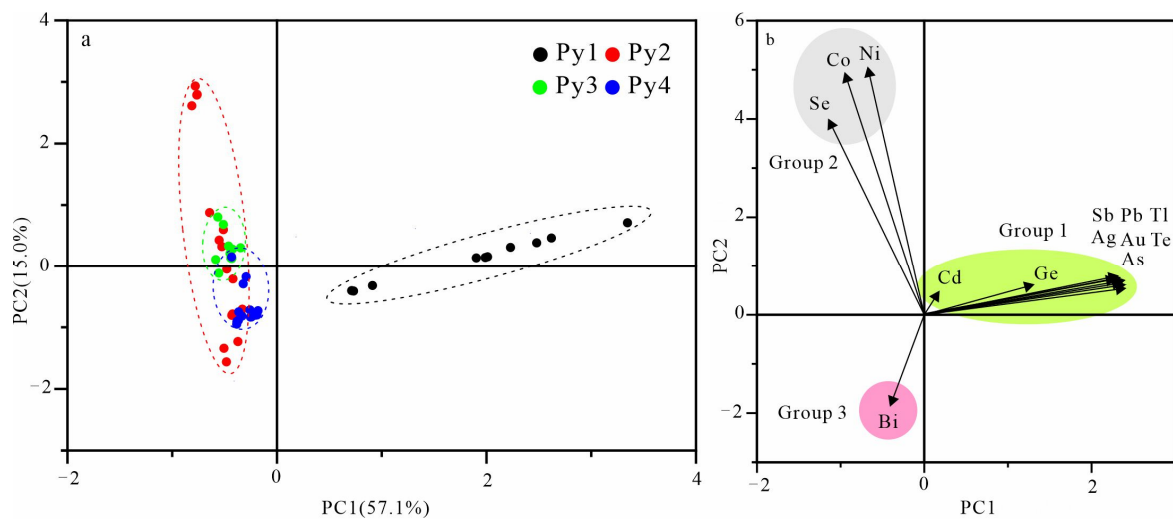


Figure 11. Results of principal component analysis (PCA) of the pyrite trace element concentrations. (a) Score plot of the first principal component (PC1 and PC2); (b) loading plot showing the elements and framed groups of elements with similar behavior.

5. Discussion

5.1. Pyrite Genesis

Cobalt and Ni are relatively common trace elements in pyrite, and the Co/Ni ratio is relatively stable in different types of deposits. The physicochemical conditions during their precipitation have a significant impact on their concentrations in pyrite; thus, variations in the Co/Ni ratios are often used to indicate differences in the genesis of pyrite [24,25]. Cobalt and Ni mainly enter the lattice of pyrite through isomorphism, and temperature has an effect on the substitution behavior of Co and Ni for Fe. Generally, the concentrations of Co and Ni in pyrite are higher at high temperatures than low temperatures [26]. The Co/Ni ratios in sedimentary pyrite are generally less than 1, hydrothermal pyrite usually has Co/Ni ratios between 1.17 and 5, and volcanic pyrite generally has Co/Ni ratios ranging from 5 to 50 [24,27]. In this paper, Py1 falls in the sedimentary zone, and Py2, Py3, and Py4 mainly are plotted in the hydrothermal zone (Figure 12). Thus, pyrites in the Jilongshan deposit mainly include sedimentary and hydrothermal genesis related to magmatism, which are the same as our results from geological and petrographic observations.

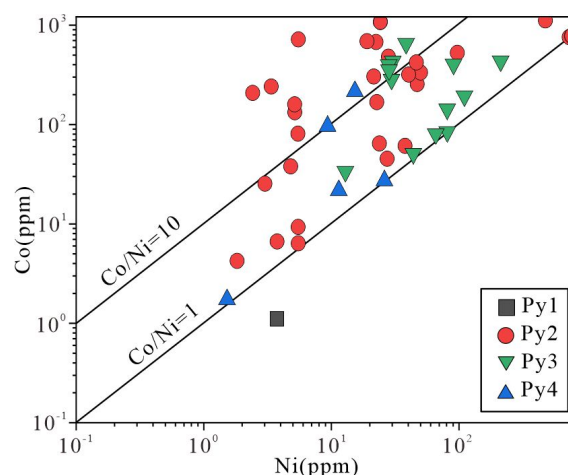


Figure 12. Binary plot of Co vs Ni in four generations of pyrites in the Jilongshan deposit [27].

Previous studies on the formation mechanism and size of framboidal pyrites suggest that the size of framboidal pyrite can reflect the redox conditions of deposition [28].

Framboidal pyrites formed in euxinic environments have an average size of 5.0 (± 1.7) μm , while in oxidic environments, it is 7.7 (± 4.1) μm [28,29]. Wignall [30] concluded that fimboidal pyrites with an average size of 7.5 μm are formed in an oxidic environment, and the maximum size is often larger than 13 μm . In this study, using statistics, the size distribution of the six areas where the fimboidal texture is relatively developed are analyzed; the statistical results are shown in Table 3. The analyzed results suggest that the average size of fimboidal pyrites in five areas (104-1-1, 104-1-2, 104-1-3, 104-2-1, and 104-2-2) are 10.0~13.2 μm , indicating that these fimboidal pyrites developed in oxidic or dysoxic environments; and the average size of fimboidal pyrites from the area 104-2-3 is 30.6 μm , indicating that this developed in a relatively higher degree of oxidic environment (Figure 13).

Table 3. Descriptive statistics of size distribution for Jilongshan fimboidal pyrite (μm).

Area	N	Mean	Median	Max	Standard Deviation	Skewness
104-1-1	292	10.0	9.7	23.4	4.18	0.56
104-1-2	64	13.0	12.6	23.0	3.81	0.17
104-1-3	125	13.2	12.6	30.0	4.19	1.01
104-2-1	64	12.9	12.9	26.8	5.43	0.31
104-2-2	121	11.9	11.3	34.4	5.19	0.85
104-2-3	14	30.6	31.5	44.5	7.70	0.11

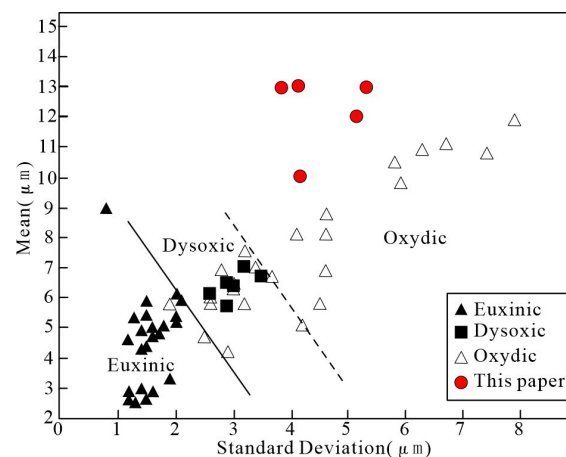


Figure 13. Binary plot of mean vs standard deviation for fimboidal pyrite from the Jilongshan deposit [28,31].

5.2. Occurrence of Se, Te, and Au in Pyrite

Previous studies have classified Se deposits into five types: magmatic, porphyry, skarn, submarine exhalation, and volcanic sedimentation [32,33]. The occurrences of Se in all ore deposits can be divided into three types: (1) existing as independent selenium minerals, such as naumannite (Ag_2Se), clausthalite (PbSe), etc.; (2) substitute to crystal lattice (S^{2-}) as isomorphism in sulphides (e.g., pyrite, sphalerite, and galena); (3) organic matter that adsorbs Se, which can occur in calcareous rocks [34–38]. The LA-ICP-MS ablation curves for Se in Py2 from the Jilongshan deposit are generally smooth, without a “peak” signal (Figure 7c,d), indicating that Se exists in the lattice of pyrite in the form of isomorphism. Electron probe results showed that Se and Ag in Py3 can reach 0.23 wt.% and 1.37 wt.%, respectively (Table 1), indicating that there might be sub-microscopic Se-bearing inclusions such as naumannite in the pyrite. Spectra of Se in Py3 also suggest that Se-Ag-bearing inclusions exist (Figure 7f).

There are two different occurrences for Te, including independent tellurides (tetradymite (Bi_2TeS_2), hessite (Ag_2Te), tellurobismuthite (Bi_2Te_3), etc.) and Te incorporation into sulfide

lattices [6,7,39]. Tellurium mainly exists in some Au deposits as calaverite (AuTe_2) and hessite (Ag_2Te); for instance, it often develops in epithermal low-temperature hydrothermal Au deposits [40]. Five different tellurides have been discovered in the Dongping Au mining area, including tetradyomite (Bi_2TeS_2), tellurobismuthite (Bi_2Te_3), petzite (Ag_3AuTe_2), altaite (PbTe), and calaverite (AuTe_2) [40]. In the Jilongshan deposit, the LA-ICP-MS analysis signals of Te in pyrite show different forms: some are relatively smooth, indicating that Te exists in the pyrite crystal structure (Figure 7c), others have the same variation trend as with Au-Ag, which may exist in the form of petzite (Ag_3AuTe_2) or other Te-Au-Ag inclusions (Figure 7h) [41]. The PCA results can also reflect the correlation of Te, Au, and Ag, particularly in Py1 (Figure 11b). The As-Te solubility curve for pyrites also confirmed the two occurrences of tellurium (Figure 14a).

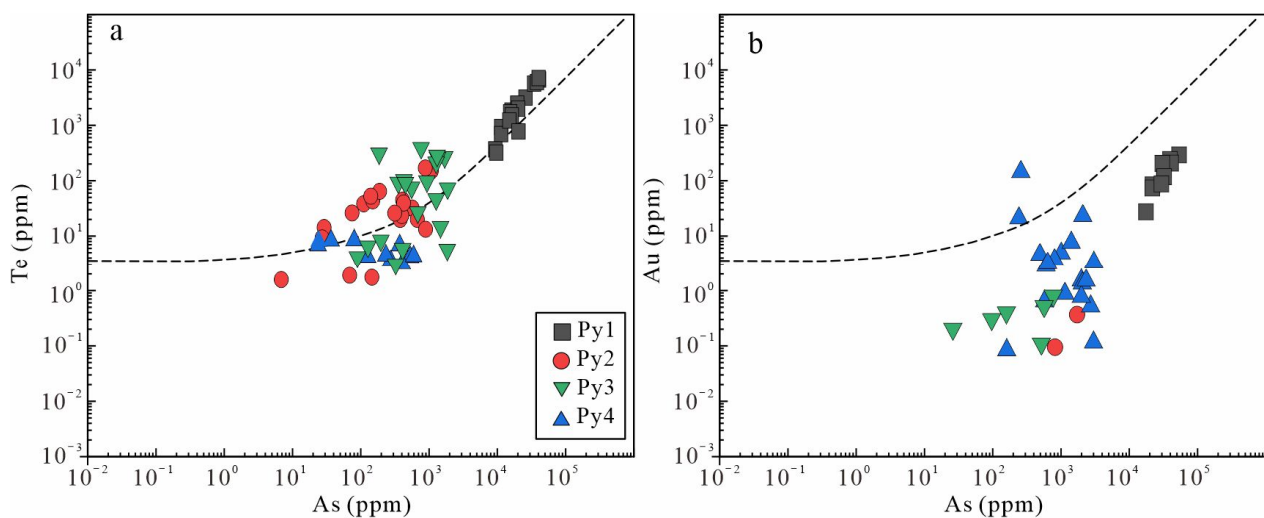


Figure 14. Concentrations of Concentrations of Te vs. As (a) and Au vs. As (b) in pyrite in the Jilongshan deposit. The black dashed line defines the solubility limit for Au (Te) solid solution in pyrite as a function of As. Gold (Te) concentrations above the solubility line indicate inclusions in pyrite [8].

Gold in many deposits have been classified into visible gold and invisible gold [6]. Based on the texture relationship between Au and sulfides, visible gold often exists by filling the cracks of other minerals or in the form of inclusions. Invisible gold can also be divided into submicron–nanometer native Au and Au^+ in the lattice [4,6]. Electron energy spectrum analyses show that native Au exists in pyrite as shown in Figure 4i; the ablation curve of Au in pyrite changes similarly to Te and Ag, indicating the existence of sub-micron to nanometer-level inclusions of Au in pyrite (Figure 7h). Further, the correlation of Au vs. As from pyrite reflects that part of Au also occurs as a solid solution in the Jilongshan pyrite (Figure 14b).

In order to deepen the understanding of Se, Te, and Au enrichment in pyrite in the Jilongshan deposit, we collected the trace elements' data of pyrite in other skarn Au-Cu related deposits in the middle and lower parts of the Yangtze River metallogenic belt, including the Baoshantao, Dongguashan, Fenghuangshan, and Xinqiao deposits [42–44]. Figure 15 shows that the Se content in pyrite from the Jilongshan deposit is obviously higher than that in other deposits. The Au contents of pyrite in Jilongshan and Xinqiao are similar, but are higher than the other three deposits. Additionally, the Te contents of pyrite in Jilongshan are higher than those in Xinqiao, as the data of the other three deposits are not compared. Therefore, pyrite in the Jilongshan is a good host mineral of Se and Te, which may generate significant economic benefits.

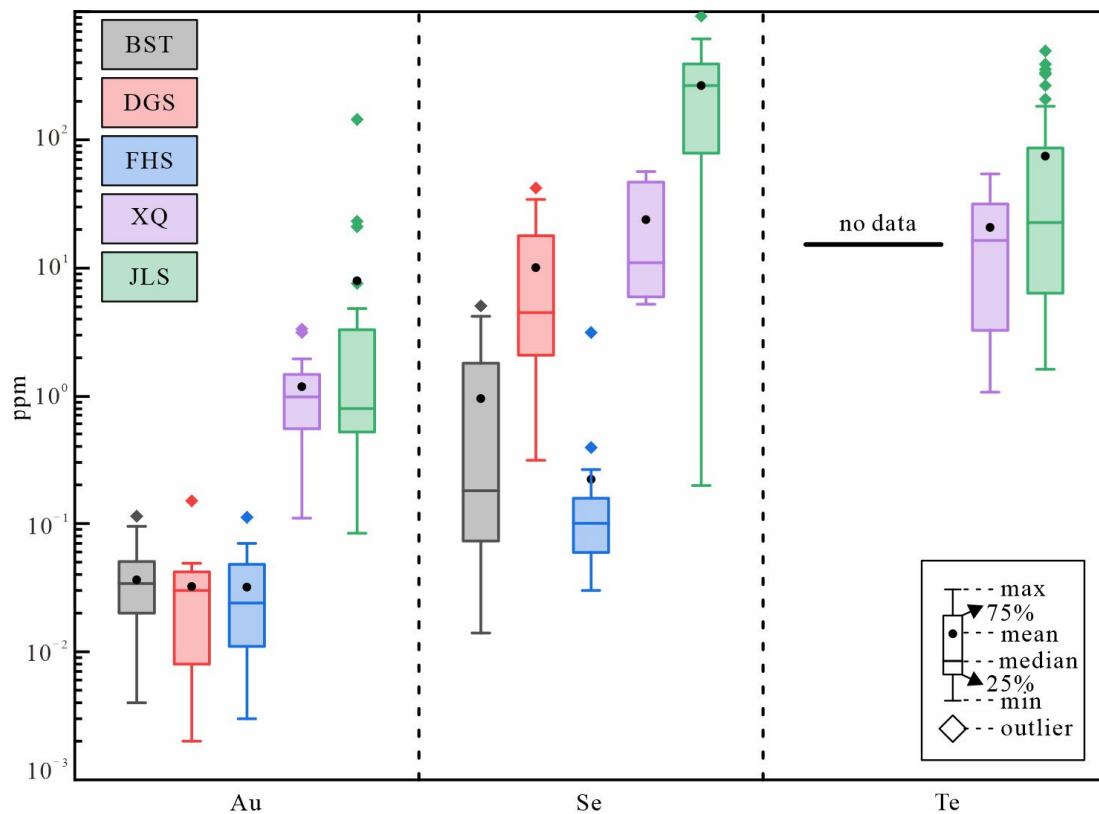


Figure 15. Comparison of Se, Te, and Au contents in hydrothermal pyrite from the Jilongshan, Baoshantao [43], Dongguashan [42], Fenghuangshan [43], and Xinqiao [44] deposits. Deposit abbreviations: JLS—Jilongshan; BST—Baoshantao; DGS—Dongguashan; FHS—Fenghuangshan; XQ—Xinqiao.

5.3. Enrichment Conditions of Se, Te, and Au

The distribution of trace elements in pyrite is affected by temperature, pressure, pH, redox conditions, and other factors. Variations in these physicochemical conditions can lead to different enrichment degrees of ore-forming elements in fluids [13–15,41]. According to the textures and compositions of different generations of pyrites, we can retrospectively analyze the evolution of pyrite, and the variations in the concentrations of trace elements in pyrite at different stages, especially Se, Te, and Au, further indicate the enrichment process of these elements. Therefore, we discuss the effects of temperature and redox conditions on the enrichment of several critical metal elements mentioned above.

(1) Temperature

Temperature plays a significant role in the precipitation of trace elements in pyrite. There is a certain correlation between Se concentrations and temperatures. Some studies suggest that the Se concentrations in pyrite will continuously increase with the rise in hydrothermal fluid temperature [45], but others think that Se-rich pyrite is formed in a low-temperature environment [46]. However, the concentration of Te in pyrite does not significantly vary with temperature changes. Gold can exist in the form of Au-Cl complexes or Au-S complexes during a wide-temperature range from below 250 °C to more than 300 °C in pyrite [47].

Previous studies have shown that high temperatures are favorable for the incorporation of Co into the pyrite lattice [48,49]. In the Jilongshan deposit, different generations of pyrite have the following Co concentrations: Py1 (median, 1.1 ppm), Py2 (median, 135 ppm), Py3 (median, 194 ppm), and Py4 (median, 5.7 ppm). Evidently, the geological phenomena show that the formation temperature of hydrothermal pyrite is higher than that of sedimentary framboidal pyrite. This is consistent with the significantly higher Co concentration measured in hydrothermal pyrite (Py2, Py3, and Py4) compared to sedi-

mentary pyrite (Py1). Moreover, the Co concentrations in hydrothermal pyrites (Py2 and Py3) are higher than that in Py4, indicating a temperature reduction trend from Py2 to Py4. This corresponds with the common coexistence of Py2 and Py3 with chalcopyrite and bornite (Figure 5h,j and Figure 6a–c), while Py4 coexists with low-temperature mineral combinations like galena, sphalerite, and covellite (Figure 6e–i). Additionally, studies on fluid inclusions in the Jilongshan deposit show that the homogenization temperatures of fluid inclusions in quartz range from 126 °C to 386 °C, with an average temperature of 286 °C; those in calcite are from 95 °C to 328 °C, averaging 222 °C, also indicating a temperature decrease from the early quartz sulfide stage to the late carbonate rock stage [18]. Further, He-Ar isotopic studies indicate an increase in the meteoric water mixing into the ore-forming fluids during the sulfide stage, which explains the causation for temperature variations in the evolution process of the ore-forming fluids [18]. Therefore, the decreased temperature in ore-forming fluids is probably caused both by the distance from the porphyry as the pyrogen and metal source and the mixing with meteoric water during the fluid migration from proximal (close to intrusive porphyry) to distal (sedimentary carbonatites).

The average Se concentrations in hydrothermal pyrites in the Jilongshan deposit are Py2 (median, 138 ppm), Py3 (median, 344 ppm), and Py4 (median, 114 ppm), respectively, which are showing a decreasing trend. As mentioned above, the formed temperatures of the Jilongshan hydrothermal pyrites reduce from Py2 to Py4, and the decreased Se contents in these pyrites suggest that a decrease in temperature is not conducive to the enriched precipitation of Se. This is consistent with previous ideas that early-stage high-temperature pyrite (Py2, Py3) is conducive to Se enrichment [45]. In contrast, the Te concentrations in different generations of pyrites are Py2 (median, 30 ppm), Py3 (median, 4.9 ppm), and Py4 (median, 90 ppm). The Au concentrations in these pyrites are Py2 (median, 0.05 ppm), Py3 (median, 0.52 ppm), and Py4 (median, 2.9 ppm), respectively. Both Au and Te in pyrite show an increasing trend from Py2 to Py4 (Figure 8). These may suggest that Te and Au mainly accumulate and precipitate in low-temperature pyrite during fluid evolution. However, the native Au precipitates in Py2 might be another reason explaining why the crystal Au contents in Py2 are less than those in Py4.

(2) Redox Conditions

Varies in redox conditions also affect the enrichment of trace elements in pyrite. Previous studies have indicated that the solubility of Te is lower in reductive fluids, and a direct cause of Te precipitation is the reduction of Te^{4+} concentration in the fluid [50]. The high concentration of Te (20,803 ppm) in pyrite collected from the Dongping orogenic gold deposit can be interpreted as being due to a sudden reduction in the oxygen fugacity of the hydrothermal fluid [12]. Keith et al. [6] found out that there is no determined relationship between Se and As in pyrites from different types of deposits and suggested that the precipitation of Se is essentially unaffected by changes in redox conditions. For Au, it is typically transported as $\text{Au}(\text{HS})_2^{2-}$ complexes, involving a chemical equilibrium $\text{Au} + \text{H}_2\text{S} + \text{HS}^- = \text{Au}(\text{HS})_2^{2-} + 0.5\text{H}_2$, and the increase in oxygen fugacity is conducive to gold precipitation [51].

In the Jilongshan deposit, the concentrations of Te and Au are highest in Py1. From the discussion in Section 5.1, it is known that framboidal pyrite forms in a dysoxic or oxidic environment. This framboidal pyrite contains the highest Au and Te contents, probably because of sedimentation, which has high background values for Au and Te. In such a case, the framboidal pyrite can be a potential source for Jilongshan Au and Te mineralization. However, based on the occurrence of Py1 in Jilongshan, the overprinted minerals (e.g., tetrahedrite, sphalerite, and galena) from hydrothermal fluids are quite obvious (Figure 4d). At present, it is therefore hard to distinguish whether the high concentrations of Au and Te are from sedimentation or late magmatic hydrothermal fluids, which needs further isotope evidence, for example, S isotope of pyrite. Nevertheless, we here focused on the redox conditions during the magmatic hydrothermal stage, which produced mainly hydrothermal pyrites (Py2, Py3, and Py4). Han and Xie [18] deduced that oxygen fugacity during the quartz-sulfide stage experienced a transition from early low oxygen fugacity to later high

oxygen fugacity according to the mineral assemblage. The concentrations of Te and Au are highest in Py4, indicating that relatively low temperature and high oxygen fugacity are more conducive to the precipitation of Te and Au as isomorphisms in pyrite. There is a strong positive correlation between Te and Au in Py4 (Figure 9e). Both single pyrite grains and the laser ablation curve (Figures 7h and 10e,f) suggest that Te-Au melts may exist in pyrite.

In summary, the evolution of different generations of pyrites can be represented in Figure 16. Framboidal pyrite (Py1) is formed during the sedimentation period with microcrystals of different morphologies. Although it contains high concentrations of Te, Au, As, and Ag, as we have mentioned above, at present, we can hardly distinguish whether it is a primary sedimentation product or it has been modified by hydrothermal fluids. More works such as S isotope need to be performed to verify this. Due to the subduction of the Paleo-Pacific plate and lithospheric stretching and thinning, large-scale magmatic underplating occurred in the Mesozoic, which also resulted in large-scale mineralization in the region [19]. During the mineralization process of skarn, due to the participation of magmatic hydrothermal fluids, the concentrations of various trace elements gradually increased in the fluids. Py1 was transformed during water–rock reactions, forming the margin of Py2 (Figure 4e). Further precipitation of ore-forming elements in the fluid resulted in the crystallization of coarse grains, euhedral Py2, which later experienced stress fracturing, with its cracks filled later by chalcopyrite (Figure 4g,h). The concentrations of As and Te within the same pyrite grain in different locations varied, while Se was relatively uniform (Figure 10c,d). As the fluid migrated further outward, the early-stage mineral (e.g., chalcopyrite) was replaced by Py3 attached to the edges or by filling its cracks (Figure 10e). Continuous precipitation of Se further led to the highest concentration in Py3. At the same time, the concentrations of Au and Te gradually increased as well. Selenium and Ni in Py2 and Py3 show a certain positive correlation and both have relatively high concentrations. With a further decrease in temperature and fluids going much farther away from the intrusion, Py4 was formed. The positive correlation between Te and Au suggests that a Te-Au melt may have formed in the fluid and moved to precipitate in Py4 (Figure 9e). In addition, the concentration of As in Py4 significantly increased compared to Py3. Arsenic and S can be combined to form $[\text{AsS}]^{2-}$, causing lattice distortion, thereby promoting the introduction of Au^+ and As^{3+} into the pyrite lattice to form invisible gold [52]. This is conducive for Py4 to become the main mineralization stage for Au and Te, which is in line with our test results.

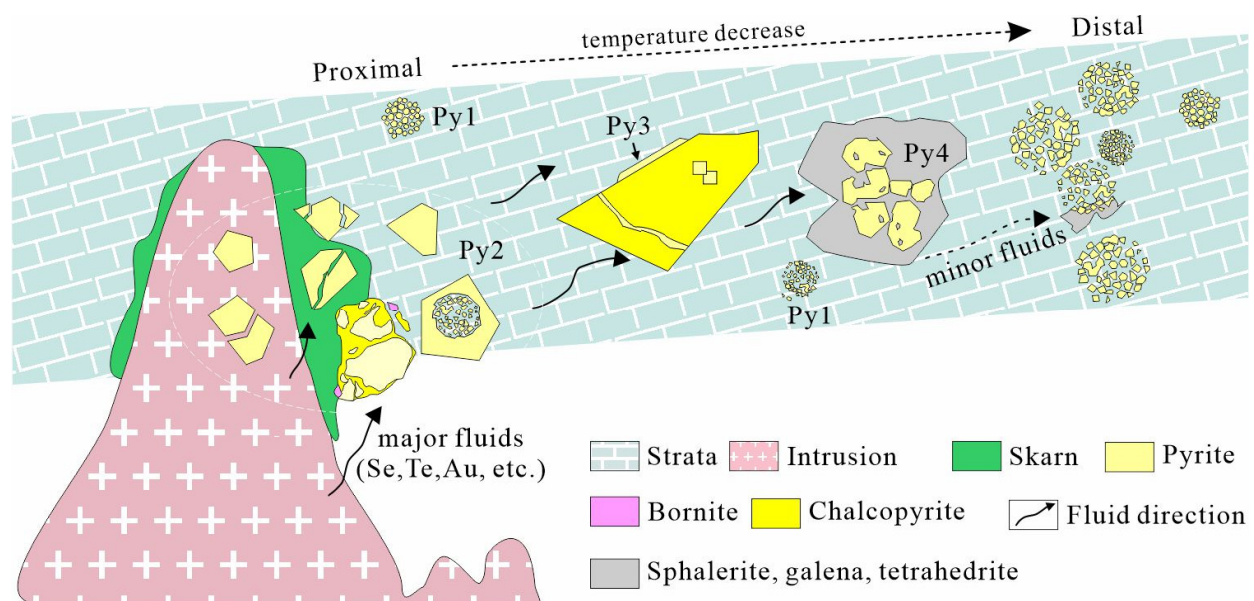


Figure 16. Metallogenic evolution model of four generations of pyrites in the Jilongshan deposit.

6. Conclusions

The following conclusions are reached:

1. The pyrite in the Jilongshan deposit can be divided into four different generations: Py1 is framboidal pyrite formed during the sedimentary period; Py2, Py3, and Py4 all belong to pyrite formed during the hydrothermal period.
2. In the Jilongshan pyrites, Se mainly occurs as isomorphism. Tellurium can occur as both isomorphism and Te-bearing inclusions. Gold mainly occurs as lattice gold and in a small amount as native Au in pyrite.
3. High temperatures contribute to the enrichment and precipitation of Se in hydrothermal pyrite, such as Py2 (median, 138 ppm) and Py3 (median, 344 ppm), while low temperatures and an increase in oxygen fugacity are conducive to the enrichment and precipitation of Au and Te in hydrothermal pyrite, particularly in Py4, which has average Te and Au concentrations of 140 ppm and 12 ppm, respectively.

Supplementary Materials: The following are available online at <https://www.mdpi.com/article/10.3390/min13121516/s1>, Table S1: Detailed information for studied samples in Jilongshan Cu-Au deposits. Table S2: EPMA data for Jilongshan pyrite (wt.%). Table S3: LA-ICP-MS data for Jilongshan pyrite (ppm).

Author Contributions: G.N., J.J. and J.X. conceived this contribution and conducted all analytical work, assisted by S.C. The manuscript was written by G.N., J.X. and W.L. with contribution from Z.C. All authors have read and agreed to the published version of the manuscript.

Funding: J.X. acknowledges support from the National Natural Science Foundation of China (Grant No. 92162217).

Data Availability Statement: The data presented in this study are available in the article and supplementary material here.

Acknowledgments: Staff at the Zijin School of Geology and Mining, Nanjing University, and Hefei University of Technology are gratefully acknowledged for their assistance with instrument operation. Thanks for the great efforts of editors and reviewers.

Conflicts of Interest: The authors declare no conflict of interest.

References

1. Gulley, A.L.; Nassar, N.T.; Xun, S. China, the United States, and competition for resources that enable emerging technologies. *Proc. Natl. Acad. Sci. USA* **2018**, *115*, 4111–41115. [[CrossRef](#)]
2. Števkó, M.; Sejkora, J.; Dolníček, Z.; Škácha, P. Selenium-rich Ag-Au mineralization at the Kremnica Au-Ag epithermal deposit, Slovak Republic. *Minerals* **2018**, *8*, 572. [[CrossRef](#)]
3. Prendergast, K.; Clarke, G.W.; Pearson, N.J.; Harris, K. Genesis of Pyrite-Au-As-Zn-Bi-Te Zones Associated with Cu-Au Skarns: Evidence from the Big Gossan and Wanagon Gold Deposits, Ertsberg District, Papua, Indonesia. *Econ. Geol.* **2005**, *100*, 1021–1050. [[CrossRef](#)]
4. Reich, M.; Kesler, S.E.; Utsunomiya, S.; Palenik, C.S.; Chryssoulis, S.L. Solubility of gold in arsenian pyrite. *Geochim. Cosmochim. Acta* **2005**, *69*, 2781–2796. [[CrossRef](#)]
5. Bullock, L.A.; Perez, M.; Armstrong, J.G.; Parnell, J.; Still, J.; Feldmann, J. Selenium and tellurium resources in Kisgruva Proterozoic volcanogenic massive sulphide deposit (Norway). *Ore Geol. Rev.* **2018**, *99*, 411–424. [[CrossRef](#)]
6. Keith, M.; Smith, D.J.; Jenkin, G.R.T.; Holwell, D.A.; Dye, M.D. A review of Te and Se systematics in hydrothermal pyrite from precious metal deposits: Insights into ore-forming processes. *Ore Geol. Rev.* **2018**, *96*, 269–282. [[CrossRef](#)]
7. Keith, M.; Smith, D.J.; Doyle, K.; Holwell, D.A.; Jenkin, G.R.; Barry, T.L.; Becker, J.; Rampe, J. Pyrite chemistry: A new window into Au-Te ore-forming processes in alkaline epithermal districts, Cripple Creek, Colorado. *Geochim. Cosmochim. Acta* **2020**, *274*, 172–191. [[CrossRef](#)]
8. Tian, H.; Xie, S.Y.; Carranza, E.J.; Bao, Z.G.; Zhang, H.; Wu, S.T.; Wei, C.H.; Ma, Z.Z. Distributions of selenium and related elements in high pyrite and Se-enriched rocks from Ziyang, Central China. *J. Geochem. Explor.* **2020**, *212*, 106506. [[CrossRef](#)]
9. Zhang, M.M.; Shen, J.F.; Santosh, M.; Li, C.L.; Liu, H.M.; Yu, H.F.; Kamoto, M.; Du, B.S.; Liu, J.J. Tellurium and gold enrichment aided by melts and pyrite crystallization kinetics: Insights from the Yongxin gold deposit, northeast China. *Ore Geol. Rev.* **2023**, *156*, 105370. [[CrossRef](#)]

10. Zhang, H.C.; Zhu, Y.F. Textural, trace elemental and sulfur isotopic signatures of arsenopyrite and pyrite from the Mandongshan gold deposit (west Junggar, NW China): Implications for the conditions of gold mineralization. *Ore Geol. Rev.* **2021**, *129*, 103938. [[CrossRef](#)]
11. Zhu, Q.; Cook, N.J.; Xie, G.; Ciobanu, C.L.; Jian, W.; Wade, B.P.; Xu, J. Gamma-enhancement of reflected light images: A rapid, effective tool for assessment of compositional heterogeneity in pyrite. *Am. Mineral.* **2021**, *106*, 497–505. [[CrossRef](#)]
12. Cook, N.J.; Ciobanu, C.L.; Mao, J.W. Textural control on gold distribution in As-free pyrite from the Dongping, Huangtuliang and Hougou gold deposits, North China Craton (Hebei Province, China). *Chem. Geol.* **2009**, *264*, 101–121. [[CrossRef](#)]
13. Peng, H.W.; Fan, H.R.; Liu, X.; Wen, B.J.; Zhang, Y.W.; Feng, K. New insights into the control of visible gold fineness and deposition: A case study of the Sanshandao gold deposit, Jiaodong, China. *Am. Mineral.* **2020**, *106*, 135–149. [[CrossRef](#)]
14. Xiao, X.; Zhou, T.; White, N.C.; Fan, Y.; Zhang, L.; Chen, X. Systematic Textural and Geochemical Variations in Magnetite from a Porphyry-Skarn Cu (Au) System and Implications for Ore Formation, Perspective from Xinqiao Cu-Fe-Au Deposit, Eastern China. *Ore Geol. Rev.* **2023**, *153*, 105271. [[CrossRef](#)]
15. Xiao, X.; Zhou, T.; Hollings, P.; White, N.C.; Fan, Y.; Zhang, L.; Fu, B. Pyrite Geochemistry in a Porphyry-Skarn Cu (Au) System and Implications for Ore Formation and Prospecting: Perspective from Xinqiao Deposit, Eastern China. *Am. Mineral.* **2023**, *108*, 1132–1148. [[CrossRef](#)]
16. Samake, B.; Xu, Y.M.; Jiang, S.Y. Oxygen fugacity, temperature and pressure estimation from mineral chemistry of the granodiorite porphyry from the Jilongshan Au-Cu deposit and the Baiguoshu prospecting area in SE Hubei Province: A guide for mineral exploration. *J. Geochem. Explor.* **2018**, *184*, 136–149. [[CrossRef](#)]
17. Han, Y.X.; Mao, J.W.; Xie, G.Q.; Bernd, L. Linkage of distal vein-type Au mineralization in carbonate rocks with Cu-Au skarn mineralization in the Fengshan area, Eastern China: Mineralogy and stable isotope geochemistry. *Ore Geol. Rev.* **2020**, *119*, 103306. [[CrossRef](#)]
18. Han, Y.X.; Xie, G.Q. Modes of occurrence of Au, Ag, Te and Bi elements and their constraint on the ore-forming physicochemical conditions of the Jilongshan skarn Au-Cu deposit, southeast Hubei Province. *Acta Petrol. Et Mineral.* **2016**, *35*, 655–676. (In Chinese with English abstract)
19. Xie, G.Q.; Mao, J.W.; Richards, J.P.; Han, Y.X.; Fu, B. Distal Au deposits associated with Cu-Au skarn Mineralization in The Fengshan Area, Eastern China. *Econ. Geol.* **2019**, *114*, 127–142. [[CrossRef](#)]
20. Pang, A.J.; Li, S.R.; Santosh, M.; Yang, Q.Y.; Jia, B.J.; Yang, C.D. Geochemistry, and zircon U-Pb and molybdenite Re-Os geochronology of Jilongshan Cu-Au deposit, southeastern Hubei Province, China. *Geol. J.* **2014**, *49*, 52–68. [[CrossRef](#)]
21. Li, X.H.; Li, W.X.; Wang, X.C.; Li, Q.L.; Liu, Y.; Tang, G.Q.; Gao, Y.Y.; Wu, F.Y. SIMS U-Pb zircon geochronology of porphyry Cu-Au-(Mo) deposits in the Yangtze River Metallogenic Belt, eastern China: Magmatic response to early Cretaceous lithospheric extension. *Lithos* **2010**, *119*, 427–438. [[CrossRef](#)]
22. Frenzel, M.; Hirsch, T.; Gutzmer, J. Gallium, germanium, indium, and other trace and minor elements in sphalerite as a function of deposit type—A meta-analysis. *Ore Geol. Rev.* **2016**, *76*, 52–78. [[CrossRef](#)]
23. Li, G.M.; Zhao, Z.X.; Wei, J.H.; Ulrich, T. Mineralization processes at the Daliangzi Zn-Pb deposit, Sichuan-Yunnan-Guizhou metallogenic province, SW China: Insights from sphalerite geochemistry and zoning textures. *Ore Geol. Rev.* **2023**, *161*, 105654. [[CrossRef](#)]
24. Braliala, A.; Sabatini, G.; Troja, F. A reevaluation of the Co/Ni ratio in pyrite as geochemical tool in ore genesis problems. *Miner. Depos.* **1979**, *14*, 353–374. [[CrossRef](#)]
25. Meyer, M.; Robb, L.; Oberthir, T.; Saager, R.; Stupp, D. Ni, Co and other trace elements in pyrite, Witwatersrand. *S. Afr. J. Geol.* **1990**, *93*, 70–82.
26. Li, F.; Zhang, G.Y.; Deng, Z.; Zhang, J.F.; Qin, Z.P.; Chen, X.; Lan, Z.W. Mineralization process of the Mazhala Au-Sb deposit, South Tibet: Constraints from fluid inclusions, H-O-S isotopes, and trace elements. *Ore Geol. Rev.* **2023**, *160*, 105595. [[CrossRef](#)]
27. Bajwah, Z.U.; Seccombe, P.K.; Offier, R. Trace element distribution, Co: Ni ratios and genesis of the Big Cadia iron-copper deposit, New South Wales, Australia. *Miner. Depos.* **1987**, *22*, 292–300. [[CrossRef](#)]
28. Wilkin, R.T.; Barnes, H.L.; Brantley, S.L. The size distribution of framboidal pyrite in modern sediments: As indicator of redox conditions. *Geochim. Cosmochim. Acta* **1996**, *60*, 3897–3912. [[CrossRef](#)]
29. Zhao, J.; Liang, J.L.; Long, X.P.; Li, J.; Xiang, Q.; Zhang, J.C.; Hao, J.L. Genesis and evolution of framboidal pyrite and its implications for the ore-forming process of Carlin-style gold deposits, southwestern China. *Ore Geol. Rev.* **2018**, *102*, 426–436. [[CrossRef](#)]
30. Wignall, P.B.; Newton, R. Pyrite framboid diameter as a measure of oxygen deficiency in ancient mudrocks. *Am. J. Sci.* **1998**, *298*, 537–552. [[CrossRef](#)]
31. Bond, D.P.G.; Wignall, P.B. Pyrite framboid study of marine Permian-Triassic boundary sections: A complex anoxic event and its relationship to contemporaneous mass extinction. *Geo. Soc. Am. Bull.* **2010**, *122*, 1265–1279. [[CrossRef](#)]
32. Simon, G.; Essene, E.J. Phase relation among selenides, sulfides, tellurides and oxides: II hermadynamic data and calculated equilibria. *Econ. Geol.* **1996**, *91*, 1183–1208. [[CrossRef](#)]
33. Simon, G.; Kesler, S.E.; Essene, E.J. Phase relation among selenides, sulfides and oxides: II. Application to selenide-bearing ore deposits. *Econ. Geol.* **1997**, *92*, 468–484. [[CrossRef](#)]

34. Xiong, Y.; Zhou, T.F.; Fan, Y.; Chen, J.; Wang, B.; Liu, J.; Wang, F.Y. Enrichment mechanisms and occurrence regularity of critical minerals resources in the Yaojialing Zn skarn polymetallic deposit, Tongling district eastern China. *Ore Geol. Rev.* **2022**, *144*, 104822. [[CrossRef](#)]
35. Kalinin, A.A. Tellurium and Selenium Mineralogy of Gold Deposits in Northern Fennoscandia. *Minerals* **2021**, *11*, 574. [[CrossRef](#)]
36. Grundmann, G.; Förster, H.J. The Sierra de Cacheuta Vein-Type Se Mineralization, Mendoza Province, Argentina. *Minerals* **2018**, *8*, 127. [[CrossRef](#)]
37. John, D.A.; Taylor, R.D. By-products of porphyry copper and molybdenum deposits. *Rev. Econ. Geol.* **2016**, *18*, 137–164.
38. Pažout, R.; Sejkora, J.; Šrein, V. Ag-Pb-Sb Sulfosalts and Se-rich Mineralization of Anthony of Padua Mine near Poličany-Model Example of the Mineralization of Silver Lodes in the Historic Kutná Hora Ag-Pb Ore District, Czech Republic. *Minerals* **2019**, *9*, 430. [[CrossRef](#)]
39. Jin, W.K.; Chen, S.Y.; Chen, J.D.; Chen, J.L.; Zhao, Y.H.; Zan, P.; Wu, R.Y. Mineralogy and geochemistry of tellurides and pyrite from the Laowan Au-Ag-Te deposit, Qinling-Dabie orogenic belt, central China: Implications for ore genesis. *Ore Geol. Rev.* **2021**, *139*, 104519. [[CrossRef](#)]
40. Gao, S.; Xu, H.; Zhang, D.S.; Shao, H.N.; Quan, S.L. Ore petrography and chemistry of the tellurides from the Dongping gold deposit, Hebei Province, China. *Ore Geol. Rev.* **2014**, *64*, 23–34. [[CrossRef](#)]
41. Gao, S.; Xu, H.; Li, S.R.; Santosh, M.; Zhang, D.S.; Yang, L.J.; Quan, S.L. Hydrothermal alteration and ore-forming fluids associated with gold-tellurium mineralization in the Dongping gold deposit, China. *Ore Geol. Rev.* **2017**, *80*, 166–184. [[CrossRef](#)]
42. Xie, J.C.; Ge, L.K.; Qian, L.; Li, Q.Z.; Sun, W.D. Trace Element Characteristics of Pyrite in Dongguashan Cu (Au) Deposit, Tongling Region, China. *Solid Earth Sci.* **2020**, *5*, 233–246. [[CrossRef](#)]
43. Xie, J.C.; Tang, D.W.; Qian, L.; Wang, Y.; Sun, W.D. Geochemistry of Sulfide Minerals from Skarn Cu (Au) Deposits in the Fenghuangshan Ore Field, Tongling, Eastern China: Insights into Ore-Forming Process. *Ore Geol. Rev.* **2020**, *122*, 103537. [[CrossRef](#)]
44. Zhou, T.F.; Zhang, L.J.; Yuan, F.; Fan, Y.; Cooke, D.R. LA-ICP-MS in situ trace element analysis of pyrite from the Xinqiao Cu-Au-S Deposit in Tongling, Anhui, and its constraints on the ore genesis. *Earth Sci. Front.* **2010**, *17*, 306–319. (In Chinese with English abstract)
45. Revan, M.K.; Gnc, Y.; Maslennikov, V.V.; Maslennikov, S.P.; Large, R.R.; Danyushevsky, L.V. Mineralogy and trace element geochemistry of sulfide minerals in hydrothermal chimneys from the Upper-Cretaceous VMS deposits of the eastern Pontide orogenic belt (NE Turkey). *Ore Geol. Rev.* **2014**, *63*, 129–149. [[CrossRef](#)]
46. Huston, D.L.; Sie, S.H.; Suter, G.F.; Cooke, D.R.; Both, R.A. Trace elements in sulfide minerals from eastern Australian volcanic-hosted massive sulfide deposits: Part I, Proton microprobe analyses of pyrite, chalcopyrite, and sphalerite, and Part II. Selenium levels in pyrite; comparison with $\delta^{34}\text{S}$ values and implications for the source of sulfur in volcanogenic hydrothermal systems. *Econ. Geol.* **1995**, *90*, 1167–1196.
47. Pokrovski, G.S.; Tagirov, B.R.; Schott, J.; Hazemann, J.L.; Proux, O. A new view on gold speciation in sulfur-bearing hydrothermal fluids from in situ X-ray absorption spectroscopy and quantum-chemical modeling. *Geochim. Cosmochim. Acta* **2009**, *73*, 5406–5427. [[CrossRef](#)]
48. Migdisov, A.A.; Zevin, D.; Williams-Jones, A.E. An experimental study of Cobalt (II) complexation in Cl⁻ and H₂S-bearing hydrothermal solutions. *Geochim. Cosmochim. Acta* **2011**, *75*, 4065–4079. [[CrossRef](#)]
49. Moh, G.H. Ore syntheses, phase equilibria studies and applications. *Neues Jb. Miner. Abh.* **1980**, *139*, 114–154.
50. Grundler, P.V.; Brugger, J.; Etschmann, B.E.; Helm, L.; Liu, W.h.; Spry, P.G.; Tian, Y.; Testemale, D.; Pring, A. Speciation of aqueous tellurium(IV) in hydrothermal solutions and vapors, and the role of oxidized tellurium species in Te transport and gold deposition. *Geochim. Cosmochim. Acta* **2013**, *120*, 298–325. [[CrossRef](#)]
51. Seward, T.M. Thio complexes of gold and the transport of gold in hydrothermal ore solutions. *Geochim. Cosmochim. Acta* **1973**, *37*, 379–399. [[CrossRef](#)]
52. Fougereuse, D.; Reddy, S.M.; Aylmore, M.; Yang, L.; Guagliardo, P.; Saxey, D.W.; Rickard, W.D.; Timms, N. A new kind of invisible gold in pyrite hosted in deformation-related dislocations. *Geology* **2021**, *49*, 1225–1229. [[CrossRef](#)]

Disclaimer/Publisher's Note: The statements, opinions and data contained in all publications are solely those of the individual author(s) and contributor(s) and not of MDPI and/or the editor(s). MDPI and/or the editor(s) disclaim responsibility for any injury to people or property resulting from any ideas, methods, instructions or products referred to in the content.